Cement and Concrete Research 210 (2026) 108394

Contents lists available at ScienceDirect

Cement and Concrete Research

journal homepage: www.elsevier.com/locate/cemconres

Early-age drying, shrinkage, and cracking in printable and printed cementitious materials☆

E. Keita [a,*], L. Denis [b,c], H. Lombois-Burger [d], S. Markin [e], Y. Weng [f], R. Wolfs [g], K. Xia [h], M. Yang [f], W. Yang [h], Q. Zhang [d], W. Zuo [h], V. Mechtcherine [i,j,k], N. Roussel [b]

[a] Navier, CNRS, Univ Gustave Eiffel, ENPC, Institut Polytechnique de Paris, Marne-la-Vallée, France
[b] CPDM/MAST, Univ Gustave Eiffel, Marne-la-Vallée, France
[c] Technical center Louis Vicat, Vicat Group, L'Isle-d'Abeau, France
[d] Holcim Innovation Center, Saint Quentin Fallavier, France
[e] Sika Deutschland CH AG & Co KG, TM Concrete, Leimen, Germany
[f] Department of Building and Real Estate, The Hong Kong Polytechnic University, Hong Kong
[g] Department of the Built Environment, Eindhoven University of Technology, Eindhoven, the Netherlands
[h] State Key Laboratory of Engineering Materials for Major Infrastructure, School of Materials Science and Engineering, Southeast University, China
[i] Institute of Construction Materials, TU Dresden, Dresden, Germany
[j] Cluster of Excellence CARE, TU Dresden and RWTH Aachen, Germany
[k] UNU Institute for Integrated Management of Material Fluxes and of Resources, Dresden, Germany

ARTICLE INFO

Keywords:
3D concrete printing
Early-age cracking
Shrinkage
Evaporation
Mitigation measures

ABSTRACT

Early-age Drying is a major source of damage in printable and printed cementitious materials, yet evaporation, capillary pressure, shrinkage and cracking are rarely considered as a unified process. This review proposes an integrated framework for drying-induced shrinkage and cracking in extrusion-based 3D concrete printing (3DCP), linking environmental, geometrical, process and material characteristics to damage evolution and performance of hardened concrete. Compared with cast concrete, deposited filaments expose all surfaces immediately and possess surface-to-volume ratios one to two orders of magnitude greater, while the high paste volumes required for extrudability amplify drying-induced deformation. In accelerated set-on-demand (2 K) systems, rapid stiffening suppresses viscous stress relaxation, potentially enabling cracking before sufficient tensile strength develops.

Drying behavior is interpreted through the competition between evaporative flux and capillary supply, governing the transition from the constant-rate to the falling-rate drying regime. This framework is supported by recent experimental advances, including digital image correlation, distributed fiber-optic sensing, near-infrared hyperspectral imaging, miniature tensiometers, and original measurements. Damage manifests initially as cracklets in the fresh state, then as propagating macro-cracks as stiffness develops. These mechanisms may also contribute to incomplete near-surface hydration, coarsened pore networks, reduced strength, weaker interlayer bond and anisotropic durability.

Mitigation strategies are reviewed across scales, from evaporation control using external curing films and biofilms to crack mitigation based on superabsorbent polymers, shrinkage-reducing admixtures and water-soluble polymer treatments. The review highlights the need to integrate systematic curing strategies, matched to both evaporative demand and to the formulation-specific vulnerability window, into 3DCP process design from the outset.

1. Introduction

Cement-based materials are manufactured at a scale exceeding 30 billion tons per year, making concrete the most widely produced man-made material on Earth [1,2]. Over the past decade, extrusion-based 3D concrete printing (3DCP) has emerged as a transformative manufacturing route, offering formwork-free fabrication, increased

☆ This article is part of a Special issue entitled: 'Digital Concrete 2026' published in Cement and Concrete Research.

* Corresponding author.
E-mail address: emmanuel.keita@univ-eiffel.fr (E. Keita).

https://doi.org/10.1016/j.cemconres.2026.108394
Received 17 May 2026; Received in revised form 24 July 2026; Accepted 2 September 2026
Available online 9 September 2026
0008-8846/© 2026 The Authors. Published by Elsevier Ltd. This is an open access article under the CC BY license (http://creativecommons.org/licenses/by/4.0/).

List of symbols

J_e	Evaporation flux at the free surface ($kg \cdot m^{-2} \cdot s^{-1}$)
J_{cap}	Capillary supply flux toward the drying surface ($kg \cdot m^{-2} \cdot s^{-1}$)
P_{cap}	Capillary pressure in the pore network (Pa)
γ	Surface tension of the pore liquid ($N \cdot m^{-1}$)
v	Mean wind speed measured ≈0.5 m above the surface ($m \cdot s^{-1}$)
p_0	Saturated vapor pressure of the concrete surface (Pa)
p_{sa}	Saturated vapor pressure of the ambient air (Pa)
RH	Ambient relative humidity (%)
k	Intrinsic permeability of the fresh paste (m^2)
μ	Dynamic viscosity of the pore fluid (Pa·s)
M	Bulk (compressibility) modulus of the fresh paste (Pa)
t_c	Characteristic poroelastic time (s)
S/V	Exposed-surface to volume ratio of the printed element (m^{-1})
w/c	Water-to-cement ratio (−)
$\varepsilon_{xx}, \varepsilon_{yy}, \varepsilon_{zz}$	Principal shrinkage strain components (−)
ε_v	Volumetric shrinkage strain (−)
σ	Internal (eigen-)stress (Pa)
m	Mass of liquid water in the sample (kg)

automation, and greater geometrical freedom [3,4]. The susceptibility of fresh concrete to early-age drying-induced damage is not, however, unique to additive manufacturing: exposed cast surfaces — most notably floor screeds — have long been recognized as vulnerable to moisture loss, capillary pressure build-up, and surface cracking, owing to their large free surface relative to their thickness [5]. Sprayed concrete (shotcrete) is an even closer precursor: large freshly sprayed free surfaces, high binder contents, and the systematic use of set accelerators expose it to pronounced early-age shrinkage and restrained-shrinkage cracking [6,7], and the accelerated stiffening it relies upon directly prefigures the set-on-demand (2K) systems. In 3DCP, the vulnerability is amplified to an extreme degree. Every face of the extruded filament is immediately exposed upon deposition, with neither the hydraulic confinement nor the evaporation barrier provided by a conventional mold.

Several characteristics of the 3DCP process amplify the drying risk beyond what is encountered even in the most exposed cast elements [5]. First, the absence of formwork means that the full perimeter of each deposited filament exchanges moisture with the surroundings from the instant of deposition; the resulting surface-to-volume ratios are one to two orders of magnitude larger than those of a structural element cast in a closed mold [8,9]. Second, printedmixtures often require a high paste volume, typically above 40% of the total volume, to ensure extrudability and buildability; since the paste phase localizes drying-induced deformation, the overall shrinkage is correspondingly large [10,11]. Third, accelerated set-on-demand systems (2K) — in which a second component, typically an accelerator, is blended into the mixture shortly before or at deposition — achieve very rapid structuration, which greatly shortens the period during which drying-induced deformation can be accommodated without damage, making these mixtures particularly susceptible to early cracking [12–14]. Beyond these material and geometric factors, on-site 3DCP is carried out under uncontrolled and potentially severe environmental conditions, which may further increase evaporation rates and the associated risk of cracking.

Printable cementitious materials are formulations meeting the rheological requirements of extrusion-based 3DCP (pumpability, extrudability, buildability); in practice, they are often characterized in laboratory set-ups without being actually printed. Printed materials mean the material effectively deposited by a printing system, the actual objective of 3DCP, to which the general statements and the consequences discussed in this review ultimately apply. This review is deliberately restricted to the material scale. Structural-scale aspects of shrinkage-induced cracking in printed structures are addressed in a companion contribution [15].

The central mechanism underpinning all phenomena considered in this review is the loss of water from the exposed surface of the fresh material. As moisture evaporates, liquid menisci recede into progressively finer pores; the resulting capillary under pressure acts as a contractile stress on the solid skeleton, driving macroscopic early-age drying-induced shrinkage [16,17]. Once the stiffening material can no longer accommodate the deformation through viscous flow, this progressive capillary loading may trigger crack initiation. Three moisture-related shrinkage regimes are classically distinguished in cementitious materials: plastic shrinkage, developing before and around setting under evaporation to the environment [16,18]; autogenous shrinkage, driven by the self-desiccation accompanying hydration and most pronounced at low water-to-binder ratios [19]; and drying shrinkage, the long-term deformation of the hardened material upon moisture loss [20,21]. This review addresses the first regime, with a scope set by the water balance rather than by the setting time: it covers the period during which moisture loss to the environment largely exceeds water consumption by hydration. The general framework thus remains applicable beyond the setting time of accelerated systems, as long as capillary water transport governs the internal moisture state: a limit that is admittedly system-dependent. Autogenous effects and long-term drying shrinkage, for which curing protocols are a well-established mitigation lever, are outside the scope of this review.

Aspects of fresh-state behavior and mix design in 3DCP have been studied [11], and mitigation strategies for shrinkage-related damage have been cataloged [22–24]. The present contribution builds on these foundations by providing a unified physical framework that explicitly connects the evaporation rate — the primary driving force — to capillary pressure, drying-induced shrinkage, and crack formation, integrating both published data and original unpublished experimental results. This framework is set out in Section 2, which introduces the causal chain that serves as a conceptual backbone for the remainder of the article. The review is then organized around three complementary perspectives. The first concerns the characterization and measurement of drying and shrinkage: the environmental, formulation, and geometrical parameters that govern evaporation are discussed in Section 3, while the experimental techniques available to quantify water loss and deformation — from global weighing to full-field digital image correlation and distributed fiber-optic sensing — are presented in Section 4. The second perspective deals with shrinkage-driven damage mechanisms, including eigenstresses, restraint effects, early-age creep, and the transition from surface cracklets to macroscopic cracks (Section 5), together with the consequences of drying-induced shrinkage on final properties such as hydration degree, pore structure, mechanical strength, and durability (Section 6). The third perspective covers mitigation strategies, from external curing films and internal curing agents to water-soluble polymer treatments and fibers (Section 7), from evaporation control to crack arrest.

2. General framework

The diverse phenomena described in this review — from evaporation kinetics and capillary pressure build-up to crack initiation and mitigation — are unified by a single physical chain rooted in the poromechanics of fresh cementitious materials [16,25], building on the classical theory of drying of porous solids [26,27]. The starting point of this chain is the ambient environment: the temperature T, relative humidity HR, and air velocity v at the exposed surface of a deposited layer jointly govern the evaporation rate J_e ($kg/m^2/s$; Fig. 1, left). The dependence of J_e on these environmental and geometric parameters — including the confinement effect of the filament geometry — is discussed

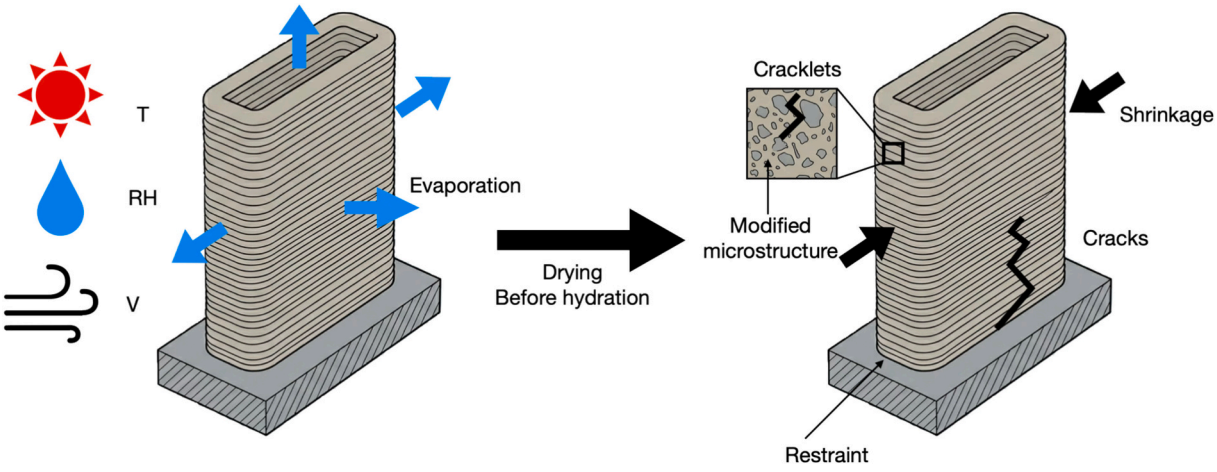


Fig. 1. General framework for drying-induced shrinkage and cracking in 3D-printed cementitious materials. Left: environmental drivers (temperature T, relative humidity HR, air velocity v) controlling the evaporation rate J_e. Right: resulting capillary pressure build-up, macroscopic shrinkage, and crack initiation.

in Section 3.3.

As water is removed from the pore network, liquid menisci recede into progressively finer pores [28,29]. The resulting capillary pressure P_{cap} is related to the local pore radius r and the liquid–vapor surface tension γ by the Young–Laplace equation $P_{cap} = 2\gamma/r$ [30]. This capillary pressure acts as an isotropic compressive stress on the solid skeleton, driving macroscopic drying-induced shrinkage (Fig. 1, right; Section 4 for measurements). In the earliest stages, when the fresh paste can still flow, deformation is largely accommodated by viscous relaxation, and the build-up of tensile stresses within the material remains limited (Section 5). This regime ends when two concurrent processes reduce the capacity for viscous accommodation: on the one hand, the granular skeleton — composed of cement particles, fillers, and aggregates — progressively densifies and percolates into a load-bearing network that limits macroscopic deformation independently of any hydration advancement; on the other hand, hydration provides additional cohesion between particles, raising the yield stress and further limiting viscous relaxation. A third possible end-point is reached when J_e drops below the rate at which capillary water can be resupplied from the interior, a transition governed by the permeability of the paste (Section 3.5). Beyond this critical window, the stiffening material can no longer deform freely in response to capillary loading. Where moisture gradients develop across the section, or where deformation is externally constrained, this differential shrinkage generates internal tensile stresses (Section 5). When these stresses, amplified by external or internal restraint, exceed the evolving tensile strength of the material, cracking initiates (Fig. 1, right). Depending on the degree of stiffening at the moment of crack onset, damage takes the form of distributed cracklets or propagating macroscopic fractures (Section 5.3). The lasting consequences of this damage on hydration degree, pore structure, and mechanical performance are discussed in Section 6; strategies to interrupt the chain at each of its links are reviewed in Section 7.

3. Early-age drying

From the instant of deposition, the exposed surfaces of a printed filament exchange moisture with the surrounding atmosphere at an evaporation rate J_e set by the ambient conditions. At the same time, the pore network of the fresh paste sustains a capillary-driven water supply flux J_{cap} directed toward the drying surface. The competition between these two fluxes determines the drying regime and the rate at which capillary pressure builds up within the material (Section 3.1). The factors governing J_e, namely temperature, relative humidity, and air velocity, are discussed in Section 3.2. The paste permeability and its dependence on formulation, which control J_{cap}, are addressed in Section 3.3. The influence of the printed element geometry and process parameters on the balance between J_e and J_{cap} is examined in Section 3.4.

3.1. Simplified classification of early-age drying regimes

The drying of a cementitious material exposed to the ambient atmosphere begins at its free surface. As long as the surface remains wet, the ambient air exerts a drying demand; for a fully saturated surface, this demand is reflected in the initial evaporation rate J_e. However, as the surface loses water, a saturation gradient develops between the drying surface and the still-saturated interior, generating a capillary pressure gradient that mobilizes pore water from the bulk toward the surface. This internal transport flux has been directly observed in model porous media [28,31–33], in soils [34], and in cementitious materials [9]. The measured evaporation rate J_e is therefore not simply equal to the ambient drying demand; it is the result of that external demand and the capacity of the material to supply water to its surface.

Two water fluxes govern this balance [28,32]. The evaporation flux J_e (kg m^{-2} s^{-1}) quantifies water demand by the environment and is well estimated by the initial rate of water loss per unit exposed area:

$$J_e = \frac{1}{S}\frac{dm}{dt}_{initial} \quad (1)$$

where S is the exposed surface area and m is the mass of liquid water in the sample. The capillary supply flux J_{cap} represents the rate at which water is transported from the interior toward the drying surface under the capillary pressure gradient; applying Darcy's law [35] across a sample of characteristic depth H gives:

$$J_{cap} = \frac{k \bullet k_r(S) \bullet P_{cap}}{\mu H} \quad (2)$$

where k is the intrinsic permeability of the paste, k_r is the relative permeability — which decreases sharply as the pore network desaturates [36] —, P_{cap} is the capillary pressure, and μ is the dynamic viscosity of water. Please note that, Darcy's law describes saturated liquid flow; once desaturation proceeds, unsaturated formulations of the Richards type provide a more accurate description of moisture transport. The relative magnitude of J_e and J_{cap} defines two distinct drying regimes.

When $J_{cap} \geq J_e$, capillary transport is sufficient to maintain a continuous liquid connection between the interior and the drying surface. This is the Constant Rate Period (CRP): the free surface remains wet, and the evaporation rate is governed entirely by external conditions (see Section 3.2), independently of the material properties. Water loss is distributed homogeneously throughout the sample depth, producing a

uniform decrease in saturation without the development of a receding dry front. Importantly, this regime does not require the presence of a surface water film from bleeding; it occurs whenever the free surface remains partially wet, and thus is supplied by internal water [28,29,37].

As saturation decreases, the effective permeability of the paste drops [36,38], reducing J_{cap}. When J_{cap} falls below J_e, capillary supply can no longer compensate for evaporation at the free surface: the system enters the Falling Rate Period (FRP). A dry region forms at the surface and advances progressively into the material; moisture transports across this dry layer then relies on vapor diffusion, which is far less efficient than liquid flow. Capillary pressure build-up and the associated shrinkage loading become concentrated near the receding wet front, localizing the stress field within the material.

The CRP-to-FRP transition is therefore controlled by the balance J_e/J_{cap}. The paste formulation plays a central role in this balance, since it determines the permeability k and hence J_{cap}; denser, less permeable pastes tend to reach the FRP onset earlier, at higher capillary pressures. It should be noted that drying and shrinkage are coupled processes: shrinkage reduces both the exposed surface area and the open porosity, which in turn affects J_e and k. However, for the deformations typical of cementitious systems, this coupling remains sufficiently limited that the orders of magnitude of the physical parameters cited above are not significantly altered [39]. The influence of the geometry of the printed element on the balance between J_e and J_{cap} is discussed in Section 3.4.

3.2. Water redistribution and bleeding

In conventionally cast concrete, shortly after placement, density differences between solid particles and water drive moisture migration upward: a process known as bleeding, that forms a surface water film [40,41]. As long as this film persists, evaporation proceeds at a rate comparable to that of a free water surface, defining the Constant Rate Period. Once the film is exhausted, negative capillary pressure builds up within the pore system, leading to internal stresses that may cause plastic shrinkage and cracking [16,18]. A critical time t_c can be defined beyond which cracking becomes possible, providing a practical estimate of the safe processing window.

Magnetic resonance imaging (MRI) allows for the internal moisture state of an opaque specimen to be mapped non-destructively and provides a direct test of these mechanisms. Fig. 2 shows the evolution of the local water content profile for a w/c = 0.35 mortar drying at a rate of 10^{-5} kg/m^2/s. During the first hour, an increase of water content is observed in the uppermost 2 mm of the sample, while the water content

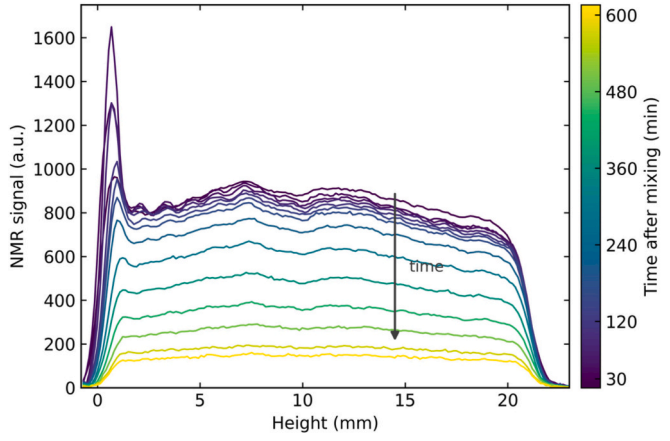


Fig. 2. Local water distribution variations as measured by MRI for a 0.35 water-to-cement ratio mortar with a drying rate of the order of 10^{-5} kg/m^2/s. Height equals zero stands for the surface of the sample. The time interval between two curves is 30 min during the first 3 h, then every hour. [Original unpublished data].

near the base simultaneously decreases: it is gravitational bleeding, as water is extracted upward from the bulk under the effect of density-driven consolidation [40,41]. After approximately 90 min, the bleeding layer recedes as the particle network consolidates and the surface water content decreases.

In printable concretes, the rheological requirements that define printability — a yield stress sufficient to resist gravitational collapse after deposition — simultaneously suppress this gravity-driven consolidation [3,42]. For the layer heights and yield stresses typical of 3DCP, gravitational body forces are negligible compared to capillary forces, and classical bleeding is expected to be strongly reduced. The extrusion process does, however, produce a lubrication layer at the filament surface where the local water-to-cement ratio is transiently elevated [43]; this localized water enrichment may contribute to sustaining surface evaporation in the early moments after deposition, but it is distinct in origin from gravitational bleeding.

Once the bleeding layer has been removed by evaporation, the water content decreases homogeneously with depth: the system is now in a regime where capillary supply from the interior — not gravitational transport — governs moisture delivery to the drying surface. The transition to the Falling Rate Period (Section 3.1) occurs when this capillary supply flux J_{cap} can no longer compensate for evaporation demand J_e, independently of any bleeding. In printable concretes, where the yield stress suppresses gravitational consolidation by design [3], this capillary-controlled regime is reached directly, without a prior bleeding phase — which is why the CRP in these materials is governed entirely by the balance J_e/J_{cap} from the outset.

3.3. Environmental parameters

3.3.1. Free flat surface

For a free, flat surface exposed to the surrounding atmosphere, the evaporation rate can be estimated using Uno's formula, derived from earlier work by Menzel on water loss from moist surfaces [44,45]. This expression relates the evaporation rate to the local thermo-hygrometric and aerodynamic conditions:

$$J_e = 8.7 \bullet 10^{-5} \cdot (p_0 - RH \bullet p_{sa}) \cdot (0.253 + 0.060v) \quad (3)$$

where:

J_e evaporation rate (kg/m^2/s),

p_0: saturated vapor pressure at the temperature of the concrete surface (kPa),

p_{sa}: saturated vapor pressure of the ambient air (kPa),

RH: relative humidity of the air,

v: mean wind speed measured approximately 0.5 m away from the surface (km/h).

Under typical laboratory or outdoor conditions, moderate temperature (20–25 °C), relative humidity between 40 and 80%, and low to moderate wind speed: Eq. (3) yields evaporation rates in the range of 10^{-4} kg/m^2/s. These values serve as a practical reference for designing experimental protocols and assessing whether on-site drying conditions are likely to affect the fresh material before the next layer is deposited [46]. Although Eq. (3) is established and widely used in concrete practice, it does not account for any specific chemistry of the material and remains valid for any wet surface. In practice, ambient conditions are rarely constant throughout the drying process, so the formula should be used as first-order estimation rather than a precise prediction. A further limitation of Eq. (3) is that it does not account explicitly for radiative heat input. Direct solar radiation raises the surface temperature of the material, and hence the saturated vapor pressure p_o, and has been shown to substantially increase pore-water evaporation, plastic shrinkage, and the severity of plastic shrinkage cracking in exposed concretes [47]. For on-site 3DCP applications without solar protection, radiative heating should be regarded as a first-order environmental parameter.

3.3.2. Effect of geometry: drying-inhibited zones

The above estimation by Eq. (3) implicitly assumes that the entire surface of the material is in contact with unsaturated air, which is rarely the case when the geometry of the specimen is confined. In a cylindrical geometry, for instance, the air trapped inside the cavity rapidly reaches saturation with respect to water vapor. Evaporation from the inner walls then becomes negligible, not because of a lack of moisture in the material, but because the vapor pressure gradient between the surface and the local atmosphere vanishes, as expressed by the $(p_0 - p_a)$ term in Eq. (3) [29].

This mechanism was investigated by Keita et al. [29] in a study of drying kinetics in a capillary channel, which demonstrated that the shape of the air/water interface directly governs the evaporation dynamics: when the interface is confined, vapor transport toward the exterior is substantially hindered and the drying front advances heterogeneously. Applied to cementitious specimens, this finding implies that only the faces directly exposed to a renewed air flow contribute significantly to mass loss. Internal lateral surfaces in a hollow cylinder, or enclosed zones in a more complex geometry, therefore dry at a much lower rate than predicted by Eq. (3) for free surfaces.

This geometric distinction is of practical importance for the design and interpretation of experimental protocols. In the specific context of 3D concrete printing, the geometry of deposited filaments and the interfaces between successive layers create locally confined zones where air renewal is limited. Applying Eq. (3) to the total surface without accounting for the effective exchange area would therefore lead to a systematic overestimation of the actual water loss [39].

3.4. Geometrical and process-related parameters

3.4.1. Layer thickness

The evaporation flux J_e (kg m^{-2} s^{-1}) is a surface quantity set by the ambient conditions (Section 3.2); it does not depend on the size of the printed element. The rate at which the total water content of the element decreases, however, scales as $J_e \bullet S/V$, where S/V is the ratio of exposed surface area to volume. For a printed filament, S/V is inversely proportional to the characteristic length of the cross-section; thin filaments therefore deplete their water content per unit volume far more rapidly than thick elements under identical environmental conditions.

This has direct consequences for the drying regime. The high volumetric drying demand of a thin filament rapidly decreases the liquid saturation, which in turn reduces the effective permeability of the paste and hence J_{cap}. The CRP-to-FRP transition, when J_{cap} first falls below J_e, is therefore reached earlier and at a higher capillary pressure in thin filaments than in thicker elements. This behavior has been observed experimentally: specimens of smaller cross-section exhibit an earlier and more pronounced rise in capillary pressure under identical conditions [8]. Consequently, both the geometry (through the S/V ratio) and the paste formulation (through its effect on transport properties) jointly govern the duration of the CRP and the onset of the FRP.

3.4.2. Multilayer deposition

In 3DCP, successive layers are deposited at time intervals that depend on the printing speed, path length, and any work interruptions [48]. Between depositions, the exposed upper surface of each layer undergoes drying: depending on the duration of the interval and the ambient conditions, this surface may partially progress into the FRP, and capillary pressure begins to build up. This partial drying progressively creates a porous, partially desaturated zone at the top of the deposited element [8]; the alteration of this layer modifies local transport properties and may compromise bonding with the subsequently deposited layer [49].

When the subsequent layer is deposited, the freshly extruded material may act as a moisture source for the partially dried surface beneath it (see Fig. 3). Whether imbibition actually occurs depends on the relative capillary state of both layers and on the quality of the contact at the interface; in some conditions, the capillary gradient is insufficient to drive significant water transfer, and the lower layer may remain in an advanced drying state.



Fig. 3. Example of deformation restraint by the underlying layer combined with moisture transport from the freshly deposited layer toward the previously deposited layer. (Adapted from [8]).

The mechanical consequences of this drying history, namely differential shrinkage between layers and the restraint imposed by the partially stiffened lower layer on the deformation of the upper layer — a restraint that is itself modulated by printing conditions — are discussed in Section 5.

3.5. Material-related parameters

As described above, from a material standpoint, drying is expected to be driven at first order by porosity, which in turn controls permeability and the capacity of the printed material to supply water to the drying surface. At second order, however, features related to material stiffness and chemical reactivity may also influence drying and its consequences.

3.5.1. Porosity and reactivity

Most printable materials are activated or chemically accelerated, meaning their reactivity at early ages is more pronounced than that of conventional cement-based materials. As a consequence, nucleation and growth of early hydrates are enhanced, alongside the dissolution of the initial phases required to sustain these reactions. Leaving aside the fact that this chemical activity generates heat, which will accelerate drying by modifying p_0 in Eq. (3), these hydrates, as their name implies, incorporate available water molecules into their crystal structure. This is particularly the case for ettringite, which forms in many set-on-demand (2 K) systems upon addition of aluminum sulfate as an accelerator. This crystal is known to incorporate 26 molecules of water per formula unit ($Ca_5Al_2(SO_4)_3(OH)_{12}\cdot 26H_2O$). It therefore converts liquid water into solid material, rapidly decreasing porosity and, consequently, permeability [50,51]. This increase in solid content stiffens the material, raising its bulk modulus and strength — enabling printability on one hand, while potentially altering its drying regime on the other.

3.5.2. Competition between contraction and desaturation

Most soft materials subjected to drying are expected to contract. It was shown in [5] that there exists an initial drying period during which the volumetric contraction of the material equals the volume of evaporated water. This indicates that, as long as the material is able to deform, it will simply contract. Beyond a critical water loss, however, the material's resistance to compression becomes sufficient to compete with the capillary stresses induced by drying, and contraction ceases. Once this threshold is reached, desaturation of the pore network — commonly referred to as “air entry” — becomes measurable.

In non-reactive systems, this transition occurs when drying-induced contraction has concentrated the solid fraction sufficiently to raise the bulk modulus to a level at which it can balance capillary stresses. In printable materials, however, the stiffening required to reach this balance is expected to be significantly influenced by the early formation of hydrates, which are independently responsible for the material's structuration and printability. Finally, the magnitude of drying-induced

shrinkage during the desaturation period that follows the contraction period is expected to scale with the inverse of the bulk modulus.

3.5.3. Drying behavior of 1K and 2K systems

One-component (1K) systems are expected to behave similarly to standard cement-based materials with respect to drying [17,52]. Following an initial contraction period — which may last several tens of minutes, during which volumetric contraction equals the volume of water lost — the system desaturates. The onset of desaturation is expected to be governed primarily by the increase in solid fraction induced by drying.

Set-on-demand (2K) systems, by contrast, are expected to undergo a rapid increase in bulk modulus and a corresponding drop in compressibility. The contraction period may be largely suppressed, which is favorable for geometrical accuracy; however, the system is expected to desaturate quickly. The rapid formation of hydrates and the fast increase in solid fraction associated with chemical acceleration may frequently place these systems in the drying regime of dry-front propagation described above.

Whether this early stiffening ultimately increases or decreases the cracking risk cannot yet be stated in general terms. On the one hand, rapid structuration suppresses viscous stress relaxation and may localize capillary loading near the drying surface; on the other hand, the same rapid hydrate precipitation builds up stiffness and tensile strength that help the material resist the increasing drying-induced stresses. The outcome is governed by the competition between capillary stress build-up and the concurrent evolution of stiffness, brittleness, and tensile strength, and likely depends on the formulation and on the drying demand. The experimental evidence base for highly accelerated systems remains too narrow to draw a definitive line; we regard this as an open research question.

4. Measurement of water loss and shrinkage

Quantifying drying shrinkage in 3DCP requires measurement of two coupled quantities: the water leaving the material and the resulting bulk and local deformations. Because printed elements are deposited in an open environment under variable climatic conditions, and because deformation gradients develop across layer interfaces, a single technique is rarely sufficient. This section reviews the methods used to characterize water loss (§4.1–§4.3) and shrinkage (§4.4), as well as the sensors that provide access to the driving thermodynamic quantity, capillary pressure (§4.6).

4.1. Estimation of water loss

Several approaches use semi-empirical methods to estimate evaporation rates and thus assess the risk of plastic shrinkage cracking. One widely known example is the ACI evaporation monograph [46], which is based on the Menzel equation [45]. This formulation assumes that evaporation from fresh concrete occurs similarly to evaporation from open water surfaces such as lakes, reservoirs, or evaporation pans. However, this assumption neglects the fundamental differences between free water surfaces and fresh concrete.

4.2. Global mass loss

Mass loss measurement through continuous weighing is a straightforward and non-invasive method to monitor drying in printed mortars, provided the balance is appropriately selected. The drying rate of fresh mortars is typically on the order of 10^{-4}–10^{-5} $kg{\cdot}m^{-2}{\cdot}s^{-1}$, meaning that mass loss is proportional to the exposed surface area of the specimen, not to its total mass (see Table 1). For a printed bead of 40–100 mm width and 300 mm length, the exposed surface ranges from approximately 0.02 to 0.05 m^2, resulting in a cumulative water loss of 70 to 180 g over 10 h. This range is well within the resolution of standard laboratory balances (0.01–1 g, capacity 0.5–5 kg) for small specimens, and remains detectable with industrial balances (resolution 1–5 g, capacity up to 60 kg) for larger printed elements. The method therefore remains applicable across typical lab-scale specimen sizes, as long as the balance capacity and resolution are matched to the expected mass loss rather than to the total specimen mass.

Table 1
Drying rates magnitudes and usual environments.

Order of magnitude of drying rates J_e ($kgm^{-2}s^{-1}$)	Equivalent conditions
10^{-4}	High wind and intense drying
10^{-5}	Enclosed and air-conditioned space
10^{-6}	Protected and minimal drying

4.3. Local water loss

In a recent study [53], near-infrared (NIR) spectroscopy was proposed as an in-line, non-destructive method to monitor moisture loss of fresh concrete during extrusion-based 3D concrete printing. The underlying principle is based on the interaction of NIR radiation with the near-surface region of a printed layer. The reflected signal contains absorption features associated with water, particularly through O—H bonds. Because the penetration depth is limited, the technique is mainly sensitive to surface moisture conditions rather than the 'bulk' water content. This makes NIR especially relevant as a real time process-monitoring tool for 3D concrete printing, where surface drying between successive deposition of layers can directly affect interlayer bond strength.

The measurement can be used as a quality control method to assess process variations, by attaching a NIR probe directly behind the nozzle (to measure the conditions of the freshly deposited layer), or in front of the nozzle (to measure the preceding layer and its conditions just before bonding occurs). Alternatively, the measurement device could be positioned at a static location or revisit certain positions multiple times, to assess the evolution of moisture content over time, i.e., during drying process.

Although the use of near-infrared spectroscopy to monitor evolution in cement-based materials is not new, prior work has focused mostly on static specimens and on longer timescales than those relevant to a typical 3D printing process. Earlier studies applied NIR to monitor cement hydration [54,55], capillary absorption and evaporation drying [56], and water concentration or penetration [57–59] up to multiple days or weeks of material age, under controlled conditions.

However, these earlier applications were generally performed with the sensor and/or specimen in a fixed measurement configuration. In such controlled environments, the illumination, stand-off distance, and surface position are either constant or well-controlled. This differs strongly from the application of NIR in a 3D concrete printing process, where the sensor is either mounted on the printhead or positioned within the printing environment to observe a continuously evolving geometry. In such a setting, the robustness of the measurement is challenging: light conditions may vary throughout the process, the distance between probe and surface can change during printing, and the target surface itself may not be constant, for instance due to progressive deformation of preceding layers. Such variations can impact the resulting absorption spectrum, and, consequently, the conversion into moisture content and its evolution.

4.4. Measurement of shrinkage at fresh state

4.4.1. Uniaxial shrinkage by laser displacement sensor

Laser displacement sensors measure the position of a target surface by triangulation of a reflected laser beam, providing non-contact, single-

axis displacement with micrometer-scale resolution. In most reported 3DCP studies, the sensor pair is mounted along the print direction so that the measured quantity is the horizontal shrinkage of the filament; a tensiometer inserted in the mix records simultaneously the capillary pressure build-up (Fig. 4). Xia et al. [61,62] used this configuration to demonstrate the constitutive link between capillary pressure increase and bulk axial deformation that underpins poromechanical modeling (see Section 5).

Laser sensor above the specimen provides access to vertical deformation, dominated by early-age plastic settlement (self-weight, bleeding); subtracting the horizontal record isolates this settlement contribution.

The principal limitation of laser displacement sensing is its unidirectional character: it captures strain along a single axis but cannot resolve shear distortion or the heterogeneous strain fields that develop at interlayer interfaces. This limitation motivates the complementary use of full-field methods.

4.4.2. Local measurement (digital image correlation)

Shrinkage in printed cementitious elements is neither uniform nor isotropic. Moisture loss varies spatially with exposure conditions, element geometry, substrate restraint, and layer interfaces, so that the three principal strain components are generally unequal ($\varepsilon_{xx} \neq \varepsilon_{yy} \neq \varepsilon_{zz} \neq \varepsilon_v/3$), with additional through-thickness gradients ($\varepsilon = f(z)$) amplified by the load of successive layers [62]. A single scalar descriptor is therefore insufficient for quality control purposes.

Digital Image Correlation (DIC) is well suited to this problem: it reconstructs full-field displacement and strain maps by tracking surface texture patterns across image sequences, with sub-pixel accuracy and no physical contact with the specimen [63]. This non-invasive character is particularly valuable for fresh mortar, for which conventional gauges are impractical, and it enables simultaneous monitoring of distributed shrinkage and crack initiation [13,64]. Out-of-plane deformation, which is invisible in planar set-ups, can be recovered using stereo-DIC with two synchronized cameras.

Applying DIC during active printing raises a specific difficulty: no single image can serve as a universal reference state since material is deposited continuously. An incremental referencing strategy — in which each image is compared to its predecessor and increments are accumulated back to the moment of deposition — addresses this challenge [24]. This approach is compatible with broader data-driven monitoring frameworks that combine optical measurements with concurrent thermal and moisture data [53].

Two complementary configurations have been implemented. At the filament scale, high-resolution DIC quantifies anisotropic shrinkage strains and detects micro-cracking as it initiates [13,24,64]. At the object scale, lower-magnification DIC tracks global shape evolution over the full drying period — including the cumulative effect of inter-layer loading on lower filaments [62], enabling real-time dimensional conformity assessment [53]. Together, these two scales provide a coherent framework connecting local material behavior to structural quality control in 3D concrete printing.

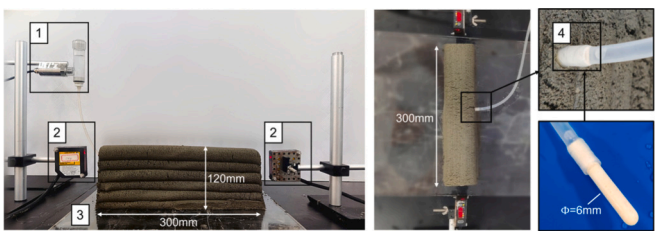


Fig. 4. Experimental setup for plastic shrinkage using the laser-displacement sensors; 1-Tensiometer; 2-Laser displacement sensors; 3-Oil covered plastic plate; 4-Ceramic probe of tensiometer (adapted from [61]).

4.5. Embedded sensors

Distributed fiber optic sensors (DFOS) measure strain distributions continuously along the embedded fiber length [65], providing a spatially resolved record of deformation that point sensors cannot deliver. When embedded in fresh concrete, the fiber captures the composite response integrating shrinkage, self-weight settlement, and thermal effects. This distributed character is particularly suited to 3DCP, where layer-by-layer deposition generates non-uniform shrinkage gradients and stress concentrations at interlayer interfaces.

In the context of cast concrete, Tan et al. [66] demonstrated DFOS crack and strain monitoring in reinforced members, and Bado et al. [67] extended the approach to shrinkage-induced strain fields over the curing period. For 3DCP, Zhang et al. [68] embedded DFOS within printed elements and tracked plastic shrinkage strains during the first 8 h, showing good agreement with image-processing displacement measurements. Key limitations include the intrusive nature of fiber embedding — which locally disrupts fresh-state flow during printing and may alter the bond at the fiber–matrix interface — and the requirement for careful fiber routing across layer joints to avoid premature debonding.

4.6. Measurement of capillary pressure

Capillary pressure in fresh concrete is measured by inserting tensiometers directly into the material, with the porous ceramic tip equilibrating with the pore water. Instruments designed for fresh-state monitoring — including the 3DCP Shrinkage Sensor [69] — consist of a control unit and capillary pressure sensors, enabling continuous monitoring of capillary pressure together with relevant environmental parameters such as solar radiation, ambient temperature, and relative humidity.

The measurable range extends to approximately 80 kPa before cavitation disrupts the water column, which covers the pressure levels typically reached during the first hours of drying in 3DCP elements operating under standard laboratory conditions. Coupling tensiometer output with gravimetric mass loss (§4.2) and laser displacement records (§4.4) allows the constitutive relationship between suction, water loss, and bulk shrinkage to be established experimentally.

When experimental access to capillary pressure is constrained by element geometry or print sequence, numerical simulation provides a complementary route [70]. Unsaturated transport models calibrated on cast specimens can be adapted to the 3DCP geometry, accounting for the exposed surface-to-volume ratio and the deposition sequence, to predict the temporal evolution of pore pressure without instrumenting each layer. The combined experimental–numerical approach is particularly relevant for multi-layer elements where sensor placement is limited to specific positions and where the full pressure field cannot be measured directly [71]. A critical limitation is that these complementary techniques are rarely measured jointly on the same printed element: cross-validated datasets combining mass loss, capillary pressure, and full-field strain under documented environmental conditions remain scarce, which limits both the benchmarking of models and the comparability of mitigation studies across laboratories.

5. Shrinkage-driven damage mechanisms

Drying shrinkage does not merely produce dimensional change: beyond a critical degree of stiffening, moisture loss generates internal stresses that can damage the material. Section 5.1 examines how moisture gradients and the layer-by-layer deposition process combine to produce eigenstresses and restraint-induced stresses. Section 5.2 discusses the role of early-age creep and stress relaxation in modulating this stress build-up, with a focus on the specific amplification mechanisms associated with 3D concrete printing. Section 5.3 describes crack initiation and morphology, distinguishing the two damage regimes

(distributed cracklets and macro-cracks) that arise depending on the material stiffness when drying exceeds its accommodation capacity.

5.1. Eigenstresses and restraint-induced stresses in early-age 3D printed concrete

The development of stresses in extrusion-based 3D printed concrete at early age is governed by the interaction of eigenstresses, originating from internal volumetric changes, and stresses induced by external or internal restraint. Both mechanisms are amplified by the specific characteristics of the 3DCP process.

Eigenstresses arise primarily from drying shrinkage. The usually high binder contents typical of printable mixtures, the absence of formwork, and the immediate multi-sided exposure of deposited filaments all promote rapid surface drying and the development of pronounced moisture gradients across the section. These gradients produce non-uniform shrinkage strains, so that the drying surface contracts more than the wetter interior; since the material is continuous, compatibility requires that tensile stresses develop near the exposed surface and compressive stresses build up in the interior. At the timescales of interest here, hydration advancement remains limited, so that the associated consumption of mixing water by the chemical reaction produces only a minor internal desiccation; this contribution to the overall stress state is neglected in what follows as a first approximation. The geometric characteristics of printed elements further intensify this effect: the deposition of narrow filaments and thin walls results in high surface-to-volume ratios, facilitating rapid moisture loss and amplifying the spatial extent of the moisture gradient relative to the total cross-section.

Superimposed on these eigenstresses are restraint-induced stresses, which are intrinsically linked to the layer-by-layer fabrication process. Each newly deposited layer undergoes volumetric changes while in contact with the layer below, which has already undergone partial drying and has acquired a certain degree of stiffness. The partially stiffened lower layer resists the deformation of the upper layer, generating tensile stresses in the shrinking upper layer and compressive stresses in the lower one. This time-dependent interaction leads to a complex stress evolution, in which both the magnitude and the location of peak stresses shift as printing progresses. The time interval between successive depositions, itself a function of printing speed and path length, directly influences the stiffness mismatch between layers and thus the intensity of restraint-induced stresses.

The degree of mechanical restraint exerted by the lower layer is not solely governed by its stiffness at the time of layer deposition, but is also conditioned by the interface quality. When the extruded filament is pressed into the previous layer, partial interpenetration increases the friction coefficient and thus the restraint. In the opposite case, when deposited from a greater height, a thin air pocket may form at the interface, reducing the effective restraint and, consequently, the magnitude of differential shrinkage-induced stresses.

5.2. Stress relaxation and early-age creep

Creep denotes the progressive time-dependent deformation under a sustained load, while stress relaxation describes the gradual dissipation of internal stresses under a constant restrained strain. In early-age cementitious materials, these two mechanisms are coupled and of the same physical origin: the viscous flow of the hydrating paste. At very early ages, when the material is still fresh or barely set, viscous accommodation is the dominant response to any applied or eigenstress, and the effective creep coefficient is orders of magnitude higher than in mature concrete. In the 3DCP context, this amplification is particularly significant: layer-by-layer deposition generates stresses from the moment of deposition, well before any significant hydration has occurred, so that the material operates in a regime of near-maximum creep susceptibility. Crucially, this early-age relaxation acts as a protective mechanism: a fraction of the eigenstresses and restraint-induced stresses described in Section 5.1 dissipates before the material has acquired the tensile strength needed to resist them, reducing the effective stress experienced by the hardening skeleton.

Several modeling approaches have been developed to quantify this interplay. Damage-rheology frameworks couple a viscoelastic constitutive law with a damage criterion to predict crack onset as a function of the stress relaxation history [72]. Burgers-type models [73], combining spring and dashpot elements in series and in parallel, provide a tractable representation of the creep response over the timescales relevant to early-age drying. Lattice models, which resolve the heterogeneous microstructure of the cement paste, capture the spatial variability of stress redistribution around pores and interfaces [74]. Across these approaches, a consistent conclusion emerges: accurate prediction of cracking risk requires explicit accounting for creep and relaxation; models that treat the fresh concrete as a purely elastic medium systematically overestimate stress build-up and thus overpredict cracking.

5.3. Cracks: cracklets/macro-cracks

When a fresh cementitious material is exposed to drying, an initial regime can be identified during which the material is deformable enough to simply shrink without any desaturation of its pore network: the volumetric contraction equals the volume of water lost by evaporation (Fig. 5) [75]. This regime persists over a characteristic consolidation time $t_c = H^2\mu/(Mk)$, where H is a characteristic dimension of the specimen, μ the dynamic viscosity of water, M the bulk modulus of the fresh paste, and k the intrinsic permeability [20,27,76,77]. In analogy with soil consolidation, t_c represents the time required for the deformation induced by the capillary pressure acting at the drying surface to propagate, by pore-pressure diffusion, across the full thickness H of the element: for timescales shorter than t_c, pressure gradients develop internally and the damage regime changes. Beyond t_c, the element deforms homogeneously as a whole. The value of t_c varies strongly with material stiffness: for a stiff mortar (w/c = 0.2, M large), t_c is of the order of seconds to less than 1 min; for a soft mortar (w/c = 0.35, M small), t_c reaches approximately 20 min.

Moreover, beyond t_c, the response bifurcates according to the stiffness of the material. In a soft material, such as a mortar with high water-to-cement ratio, the compressibility modulus is low, so that capillary pressure is sufficient to extract water from the matrix and drive consolidation and reorganization of the solid skeleton. Water loss in this regime is concentrated at the free surface, where evaporation first exceeds capillary resupply. The resulting damage takes the form of cracklets: shallow, distributed features with aspect ratios of order ten and widths of several hundred micrometers, formed by capillary-pressure-driven reorganization of the paste rather than by classical fracture mechanics (Fig. 6a) [78]. In a stiff material, such as a mortar with low water-to-cement ratio, the skeleton resists consolidation and water cannot be extracted from the matrix by capillary action. Instead, a pressure gradient builds up between the drying surface and the wetter interior; this gradient generates macroscopic tensile stresses that, once they exceed the evolving tensile strength of the material, produce macro-cracks propagating from the surface inward (Fig. 6b) [5,49]. These macro-cracks are morphologically similar to drying cracks observed in hardened concrete. A full quantitative analysis of the damage statistics extracted from these tomographic images (crack opening, depth distributions, and affected volume fractions as a function of w/c) is provided in [5]; Fig. 6 is reproduced here to establish the morphological distinction between the two regimes.

The implications for 3D concrete printing are significant. Printable materials are typically soft at early age, by design, since sufficient deformability is required for extrusion and layer-on-layer buildability. This places them firmly in the cracklet regime: the three necessary conditions (soft matrix, homogeneous water loss, sufficient water loss) are generally met in the minutes following deposition. The printed

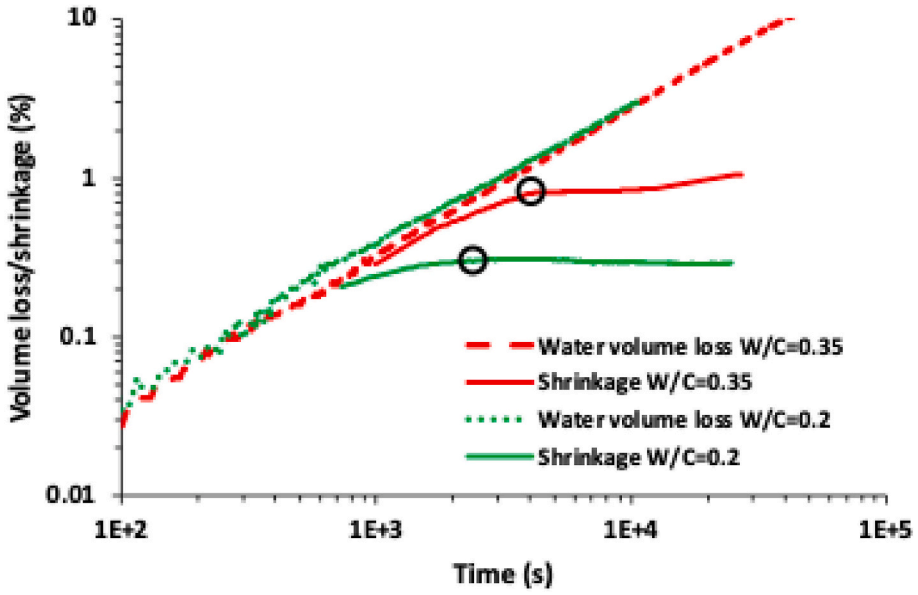


Fig. 5. Comparison between the average drying-induced shrinkage measured using microtomography and the volume loss corresponding to the measured water loss for the two mortar samples. The white dots show the first observation of microstructural damages in fresh samples. (Adapted from [5]).

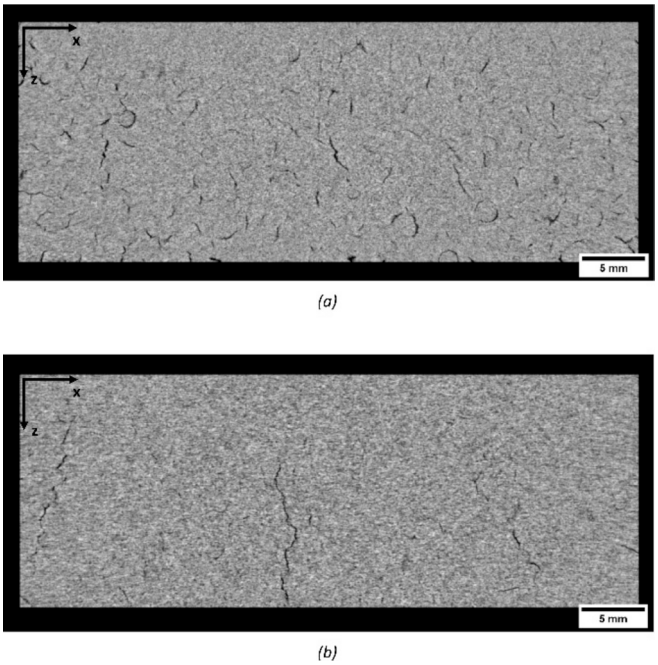


Fig. 6. Distribution over depth of the microstructural damages obtained through subtraction of tomographic images of the initial state and after 2.5 h drying: (a) W/C = 0.35; (b) W/C = 0.2. (Adapted from [5]).

geometry reinforces this tendency, since the high surface-to-volume ratio of deposited filaments promotes rapid surface drying before the material has stiffened. Whether the eventual damage remains confined to distributed cracklets or evolves into macro-cracks depends on the rate at which stiffening, driven by percolation and hydration, outpaces the continuing drying demand.

6. Consequences on final properties

The early-age drying history described in Sections 3 to 5 leaves persistent fingerprints on the hardened state of a printed element. The present section examines how this early-age history translates into lasting differences in the final properties of the printed element: the degree of hydration (§6.1), the bulk mechanical performance and interlayer bond (§6.2), the pore structure and associated mechanical anisotropy (§6.3), and the transport properties that govern long-term durability (§6.4).

6.1. Incomplete hydration

The total water lost by evaporation from a printed element remains small relative to the initial mixing water content. Considered as a bulk average, this loss would cause only a modest reduction in the effective water-to-cement ratio and would have limited consequences for the overall degree of hydration. However, evaporation is not uniform: it is concentrated at the exposed surface of the deposited layer, where the absence of formwork creates a continuous free surface in contact with the ambient atmosphere. In low water-to-cement ratio formulations, this localized loss is sufficient to substantially deplete the water available for hydration reactions in the near-surface region [49,79]. The transition to the falling-rate drying regime, in which the drying front recedes into the material rather than advancing from the free surface, further amplifies this depletion at higher evaporation rates, shorter resting times, or lower water-to-cement ratios.

The consequence is a gradient in the degree of hydration across the filament cross-section: the near-surface region, where the loss is concentrated, reaches a lower final degree of hydration than the interior, leaving behind a more porous matrix with reduced cementitious binding capacity. This surface hydration deficit accumulates over successive layers and is a primary driver of the mechanical and durability penalties described in the following subsections.

6.2. Mechanical performance

Without active curing, evaporative water loss can exceed the water consumed by chemical hydration during the first hours, leading to a rapid decrease of the internal relative humidity within the filaments [80]. Once this internal relative humidity drops below approximately 80%, cement hydration kinetics slow markedly [81], and the formation of hydration products becomes insufficient to fill the capillary porosity inherited from the mix design. The resulting matrix is characterized by a

coarser pore size distribution than that of a properly cured concrete of identical composition [80,82].

This hydration deficit compounds with process-specific features of extrusion-based 3DCP. The extrusion step itself tends to elongate pores and increase the connectivity of the capillary network relative to cast concrete of similar mix design. When drying occurs before hydration has sealed this network, the unfilled and interconnected porosity constitutes a population of pre-existing flaws that facilitates crack propagation under load [80,83]. The macroscopic consequence is a reduction of compressive and flexural strengths typically reported in the range of 20 to 30% for specimens dried under standard ambient or mild wind conditions, compared to properly cured references [80,84]. Beyond bulk strength, surface drying also impairs the interlayer bond: as the upper surface of a freshly deposited filament dries during the resting time before the next layer is placed, the bonding capacity at the interface decreases, and this decrease becomes significant once the surface has dried to a degree that prevents adequate intermingling of the fresh and partially stiffened materials [79,85]. These effects are inherently coupled, and active curing is therefore a prerequisite for both reproducible bulk strength and reliable interlayer cohesion in formwork-free fabrication.

6.3. *Pore structure distribution: pore shape, pore volume and mechanical anisotropy*

In practical printing conditions, the plastic shrinkage deformation of a printed element is not freely developing but is partially restrained by the substrate and by the surrounding structure. This restraint produces a non-uniform distribution of shrinkage strains across the element [3,4], which in turn modifies the local pore structure. Recent work by Xia et al. [86] provides a quantitative characterization of this coupling, comparing specimens printed under free deformation conditions and specimens with deformation constrained at both ends and the bottom. Systematic differences in pore volume emerge between the two cases: pores larger than 4 mm^3 appear in the constrained specimens but are absent under free deformation, and the pore volume measured under constraint is consistently higher across all pore sizes, with the difference amplified at larger scales (Fig. 7). Constrained plastic shrinkage thus produces a pore-coarsening effect whose intensity scales with the level of external restraint.

Superimposed on this volumetric effect, the extrusion process itself generates anisotropic pore shapes. The compressive and stretching actions at the nozzle produce pores that are systematically elongated along the printing direction [5]. Sphericity, defined such that unity corresponds to a perfect sphere, is therefore reduced in as-printed material relative to cast concrete. During the hours following deposition, the viscoelastic response of the fresh paste allows partial recovery of pore sphericity; however, this recovery is progressively suppressed as external restraint increases and as surface drying accelerates pore structure freezing, so that doubly constrained specimens retain substantially lower sphericity values than freely deforming or surface-covered ones (Fig. 7c). The bottom region of each element, subject to additional restraint from gravity and friction with the print bed, consistently shows the largest sphericity reduction. Because pores elongated along the printing direction preferentially reduce strength in the two perpendicular directions, the suppression of sphericity recovery translates directly into more pronounced mechanical anisotropy: elements subjected to stronger constraint display higher anisotropy coefficients for compressive strength, as illustrated in Fig. 7.b. Constrained plastic shrinkage therefore affects not only the bulk strength of printed elements through its contribution to early-age cracking, but also the directional distribution of their final mechanical properties.

6.4. *Durability*

Early-age drying affects the long-term durability of printed elements through two coupled mechanisms: modification of bulk transport properties and specific alteration of the interlayer interfaces. In the bulk, shrinkage-driven microcracking and the hydration deficits described in Sections 6.1 and 6.2 produce a pore network that is both coarser and more connected than in a properly cured cast concrete of equivalent composition. The absence of compaction, inherent to extrusion-based 3DCP, further increases this connectivity relative to standard concretes [87]. As a consequence, water absorption (sorptivity), carbonation depth, and chloride ingress rates are all elevated in printed materials compared to cast equivalents, as documented in a recent RILEM TC 304-ADC interlaboratory study conducted on a range of printable mixes [88]. An additional specificity of 3DCP is that these

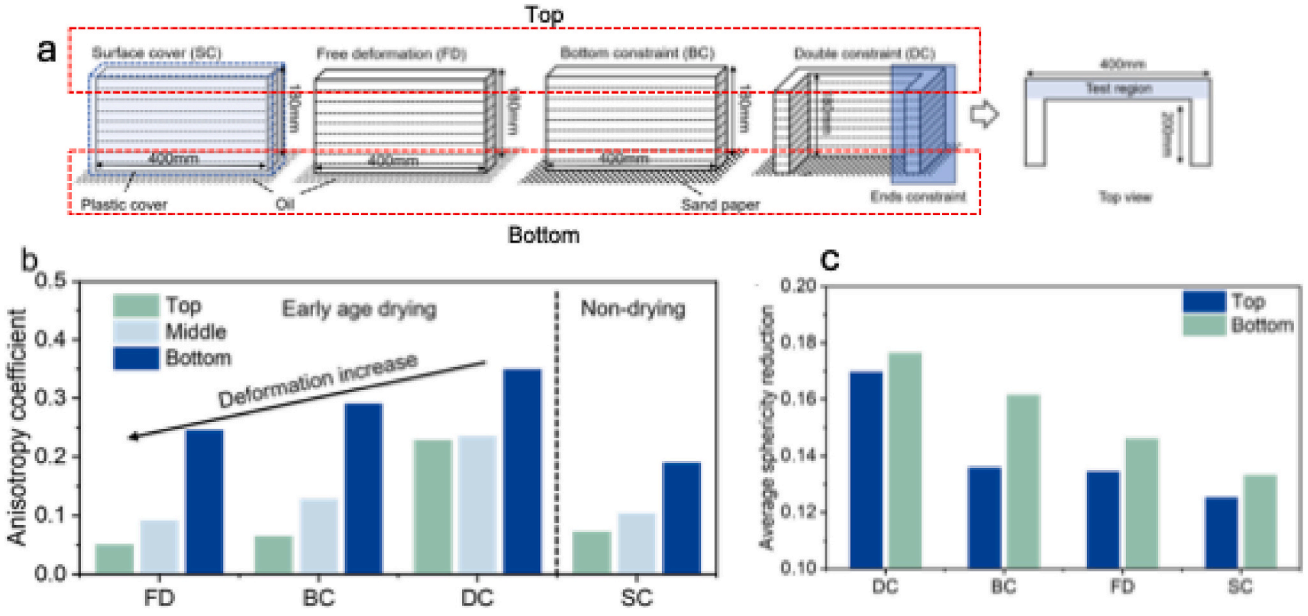


Fig. 7. Effect of plastic shrinkage under different constraint conditions on the pore size and shape distribution in 3DCP: (a) schematic of the four constraint conditions studied: FD (free deformation), SC (surface cover), BC (bottom constraint), DC (double constraint); (b) anisotropic coefficient of compressive strength; (c) pore sphericity reduction. (Adapted from [86]).

transport properties are anisotropic: the layered microstructure produces directional differences in sorptivity, carbonation rate, and chloride ingress that have no equivalent in isotropic cast concrete [88–90]. For reinforced printed elements, this anisotropy and the generally reduced cover thickness of filament-based sections make early-age drying a first-order parameter for service-life design.

At the interlayer scale, the upper surface of each deposited filament is exposed to ambient drying during the resting time before the next layer is applied. When this interval is long enough to cause partial setting or surface desiccation, the resulting interface can behave as a cold joint, defined as a discontinuity characterized by insufficient intermingling and bonding between successive filaments [87]. Cold joints constitute preferential pathways for aggressive agents: local carbonation depth and chloride ingress at the cold joint can significantly exceed the values measured in the bulk material away from the interface [91]. The severity of this effect scales with the filament interval time, since the degree of drying and stiffening of the lower layer increases before the next layer is deposited. For moderate resting times, a partial compensation may arise: evaporative drying reduces the local effective water-to-cement ratio at the filament surface, which, once a reliable bond is established, may locally improve transport resistance. The balance between these competing effects is non-monotonic in resting time and has not yet been fully characterized for representative mixes; the recent development of standardized durability testing protocols by RILEM TC 304-ADC provides a basis for systematic investigation [87,92].

7. Mitigation strategies

The General Framework (Section 2) identifies several points at which the progression from pore-water suction to cracking can be interrupted. Mitigation strategies in 3DCP can accordingly be grouped into two complementary families. Strain-limiting interventions target the physical driving force itself by reducing the evaporative flux, postponing menisci recession, lowering the capillary pressure, or compensating the volumetric contraction. Stress-managing interventions, in contrast, accept that a degree of shrinkage is unavoidable and instead modify the mechanical boundary conditions and fracture resistance to suppress crack initiation despite shrinkage. Within these two families, each technique can be classified more finely by the specific mechanism through which it acts:

- reducing the evaporative flux J_e at the free surface (external curing),
- increasing the capillary supply J_{cap} or postponing menisci recession (internal curing),
- decreasing the capillary pressure P_{cap} itself through surface-tension reduction (shrinkage-reducing admixtures),
- compensating the volumetric contraction (expansive agents),
- or accepting the strain and limiting its mechanical consequences (fiber reinforcement, polymer networks, geometric and process design).

Each of these mechanisms corresponds to a specific link of the causal chain of Fig. 1, and thereby to specific consequences documented in Section 6. Strategies that reduce the evaporative flux or sustain the capillary supply postpone capillary-pressure build-up and thus act simultaneously on shrinkage and cracking (Section 5) and on the near-surface hydration deficit and its mechanical and durability penalties (Section 6). Stress-managing strategies, by contrast, leave the water loss largely unaffected: they act specifically on crack initiation and propagation (Section 5.3). It should be stressed, however, that several of the strategies reviewed below were developed empirically, and their assignment to a single mechanism of the causal chain is not always supported by direct experimental evidence.

Indeed, mitigation in 3DCP is constrained by the printing process. Printable mixtures must simultaneously satisfy pumpability, extrudability and buildability, so the dosage windows routinely used in cast concrete are typically narrower; dosage that mitigates shrinkage often alters the yield stress, the structural build-up rate or pump stability [3]. Economic considerations further restrict the practical envelope [3,4,93]. The sub-sections that follow address external curing (§7.1), internal curing (§7.2), reinforcement and volumetric compensation (§7.3), water-soluble polymers (§7.4), and process and design-based mitigation (§7.5).

7.1. External curing

7.1.1. Classical external curing

External curing targets the evaporative flux J_e directly by interposing a barrier, or by lowering the vapor-pressure gradient at the free surface. The simplest measures, polyethylene (PE) covering, water misting, and the application of curing compounds, are inherited from conventional cast concrete practice but behave differently on printed elements. Covering a freshly printed element with PE foil raises the local relative humidity and retards evaporation, but the non-planar surfaces generated by extrusion leave residual gaps between the foil and the substrate, through which water accumulates and eventually re-evaporates [8,23]. Covering also interferes with continuous printing and requires additional handling unless automated. Water misting, whether applied once or at regular intervals, is more compatible with the process but only transiently effective: Moelich et al. [23] reported that a single water spray reduced the 3-hour plastic shrinkage by only 6%, whereas repeated misting at 20-minute intervals increased the reduction to 19%. Curing compounds offer a more robust alternative: Moelich et al. [23] measured a 34% reduction of 3-hour free shrinkage upon application of a commercial curing agent, and Markin and Mechtcherine [64] reported that a paraffin-based curing compound delayed the onset of capillary pressure build-up in a printed wall by approximately 1.1 h and reduced the horizontal shrinkage strain by a factor of three relative to the uncured reference.

7.1.2. In-situ crosslinked bio-films

The practical limitations of PE foils on 3D-printed surfaces have motivated the development of external curing agents that self-conform to the freshly printed geometry. Xia et al. [60] proposed spraying a sodium-alginate (SA) solution on the surface of the extruded filament: SA, a non-toxic biodegradable polysaccharide, spontaneously crosslinks with the Ca^{2+} ions leached from the fresh cementitious surface to form a continuous water-retaining film in-situ. Because crosslinking occurs at the real surface of the printed element, the film conforms to the corrugated geometry and suppresses the residual gaps observed under PE covering (Fig. 8 a, b). The underlying mechanism is the same as for conventional covering, reducing J_e, but with substantially improved surface contact (see Fig. 9 and Fig. 10).

7.1.3. Nano-silica modified alginate (NSSA)

The SA films produced by Ca^{2+} crosslinking alone retain a porous structure that limits their water-retention efficiency. Xia et al. [60] addressed this by incorporating nano-silica (NS) into the SA solution: hydroxyl groups at the NS surface interact with those of the SA chains and reduce the film permeability, while residual NS particles can further react with $Ca(OH)_2$ at the cement surface to form C-S-H and densify the film-substrate interface (NSSA, Fig. 9). Under reference evaporative conditions, post-print spraying of NSSA reduced the 24-h plastic shrinkage of 3DCP by about 60%, the capillary pressure at 180 min by about 70%, and the 24-h cumulative water evaporation by about 75% (Fig. 10) [60]. Although these values approach those obtained with polymer-incorporated strategies (§7.4), the bio-film route preserves the original mix design and acts only on the surface, which is an operational advantage when mix compatibility is constrained.

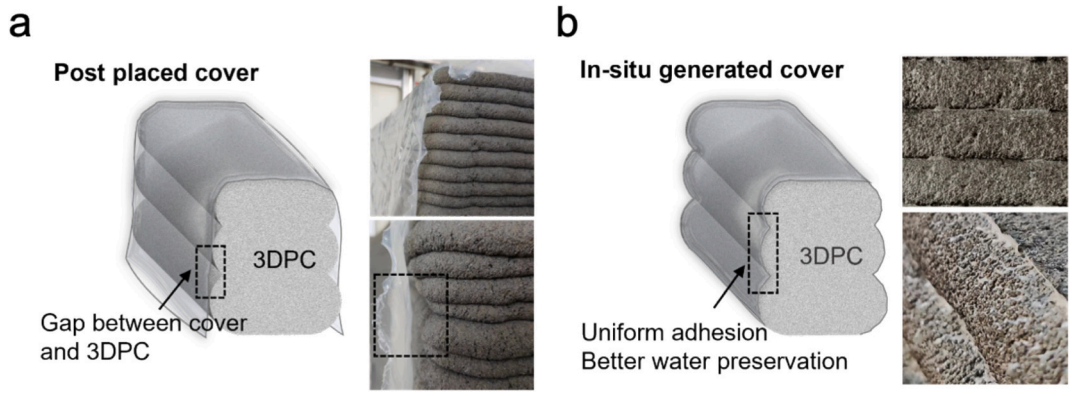


Fig. 8. Comparison between the (a) traditional post placed plastic film cover and (b) in-situ generated cover on the 3DCP surface for moisture-retaining.

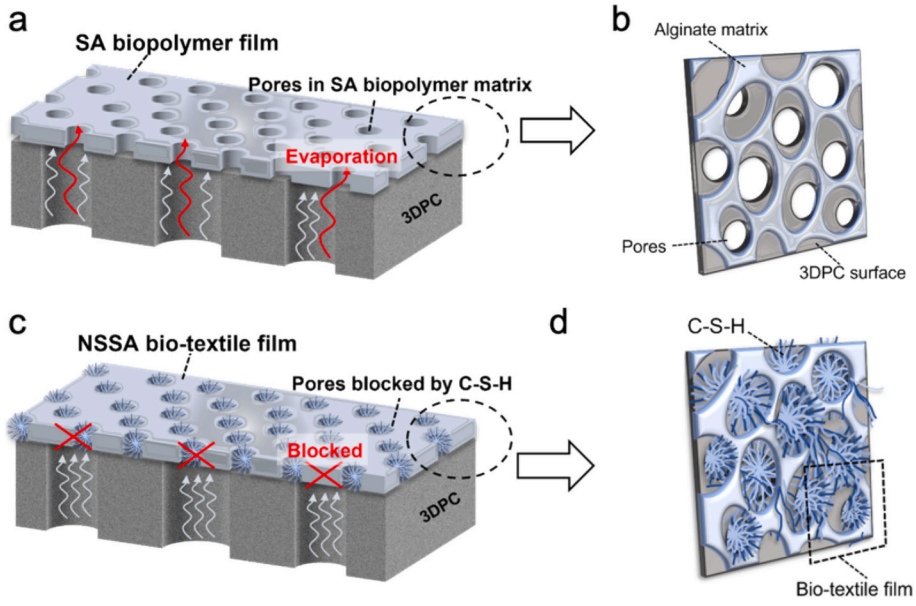


Fig. 9. Structure of water-retaining film generated by sodium alginate (SA); (a–b) traditional SA crosslinked film with porous structure; (c–d) Nano silica modified SA (NSSA) crosslinked film with blocked structure and further entangled C-S-H gels.

7.2. Internal water reservoirs and surface-tension reduction

7.2.1. Superabsorbent polymers

Superabsorbent polymers (SAPs) absorb part of the water during mixing and release it back into the cementitious matrix as hydration and self-desiccation progress [23,24,94]. In terms of the general framework of Section 2, SAPs act on the capillary supply J_{cap}: by sustaining a local water source within the paste, they delay the onset of capillary pressure and the associated menisci recession. The use of SAPs for internal curing against autogenous shrinkage has been codified in the RILEM TC 260-RSC recommendation [94]. This mechanism is unambiguously effective against autogenous shrinkage, for which Van Der Putten et al. [24] reported reductions of up to 200% in printed OPC mortars, and Chen et al. [95] showed sustained expansion up to 7 days in LC3 pastes. Evidence regarding plastic shrinkage in 3DCP is more nuanced. Moelich et al. [23] observed that self-releasing SAPs had no significant effect on the 3-hour plastic shrinkage, because their release rate was slow relative to the evaporation rate (the estimated water demand exceeded the actual release by more than a factor of five), whereas SAPs with demand-controlled desorption, which releases water in response to matrix contraction, reduced the 3-hour shrinkage by 10%. Beyond the purely shrinkage response, SAPs modify the rheology and stiffening kinetics of printable mixtures [22,23], and their use in foam concrete is also constrained by the bubble volume fraction, which governs early-age shrinkage [22]. The net benefit in 3DCP is therefore dosage- and SAP-type-dependent, and requires joint optimization with the rheological requirements.

7.2.2. Shrinkage-reducing admixtures

Shrinkage-reducing admixtures (SRA) act through a distinct mechanism: the surface tension γ of the pore liquid. Because the capillary pressure developed in partially saturated pores scales as $P_{cap} = 2\gamma/r$ (§2), a reduction of γ by 20 to 40% typical of glycol-ether-based SRAs translates directly into a proportional reduction of the driving pressure for plastic and drying shrinkage, without any change in the water content or hydration kinetics [96]. Under this framework, SRAs are conveniently treated as a chemical form of internal curing, since they modify the internal pore fluid rather than the external boundary conditions. Their efficacy is well documented in cast concrete, where dosages of 1 to 2% by mass of cement reduce long-term drying shrinkage by 30 to 50% [97,98] and significantly reduce the severity of plastic shrinkage cracking [99]. In 3DCP, however, two complications blur this picture. First, many printable formulations already contain glycol-ether-based rheology modifiers, so that part of the SRA effect is implicitly present before any dedicated SRA is added. Second, the dosage window is constrained by buildability: Moelich et al. [23] reported that at 1%

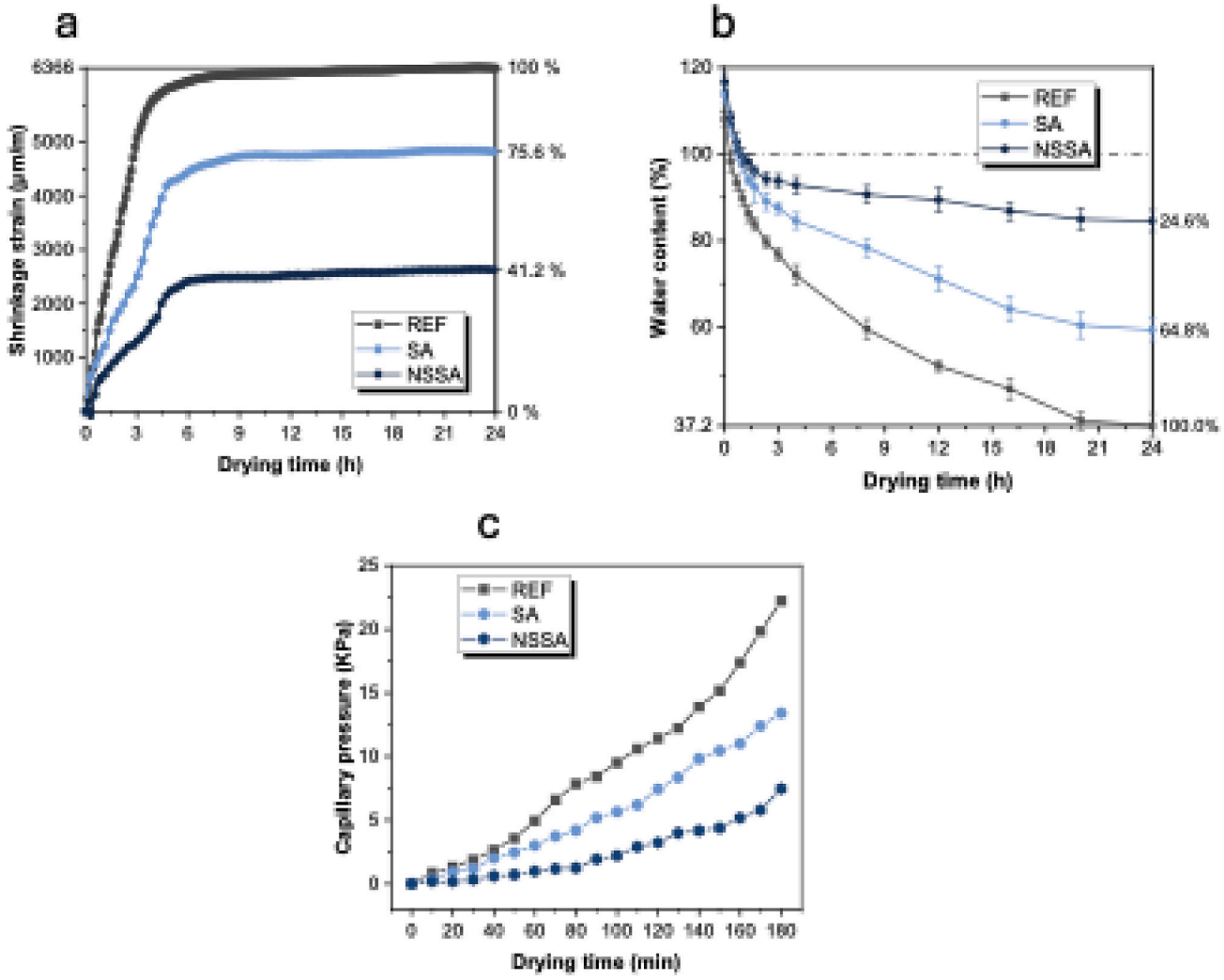


Fig. 10. Water retaining and shrinkage mitigation effect of SA and NSSA film on 3DCP; (a) Plastic shrinkage curves within 24 h after printing completion; (b) Plastic shrinkage curves within 180 min after printing completion; (c) Capillary pressure within 180 min after printing completion; (d) Change of water content within 24 h after printing completion; (e) Change of water content within 180 min after printing completion.

dosage a glycol-ether SRA produced no statistically significant reduction of the 3-hour plastic shrinkage, and that higher dosages compromised buildability and were not printable with their reference mixture. The rheological coupling between surface-tension reduction, air entrainment, and yield-stress evolution is therefore the key determinant of whether an SRA is effective in 3DCP, and the experimental evidence base is still too limited to prescribe generic dosage ranges.

7.3. Reinforcement and volumetric compensation

7.3.1. Microfiber reinforcement

Microfiber reinforcement does not directly address the physical drivers of shrinkage. Instead, it acts downstream of the strain: by providing bridging forces across incipient cracks and redistributing tensile stresses, fibers raise the post-cracking tensile capacity and limit crack initiation and propagation [83,100]. Two specificities of 3DCP are relevant here. First, extrusion aligns the fibers preferentially along the flow direction, which is also the direction most vulnerable to plastic shrinkage cracking in elongated printed elements. Ma et al. [100] quantified this anisotropy by cutting specimens parallel and perpendicular to the printing direction and measuring lower total shrinkage and cracking on the aligned specimens. Second, fiber addition interacts with pumpability: fiber length and dosage must remain compatible with the pump and nozzle, which in 3DCP converges on short fibers at modest dosages. Within this envelope, Moelich et al. [83] showed that short polypropylene monofilament (6 mm) eliminated early-age cracking of printed mortar prisms without adverse effect on mini-slump flow. In the specific context of 3DCP, the combination of natural fiber alignment along the critical cracking direction and short-fiber pumpability makes microfibers the most directly effective mechanical mitigation of shrinkage cracking available to date, with the clear caveat that fibers do not reduce the shrinkage strain itself.

7.3.2. Volumetric compensation

A complementary approach is to compensate the volume reduction through expansive phases or a modified clinker chemistry, rather than prevent it. Chen et al. [101] reported that magnesium oxide-based expansive agents had a limited effect at very early ages but significantly restrained drying shrinkage at later ages, a time-dependent response consistent with the delayed hydration and expansion kinetics of dead-burned MgO. Calcium sulfoaluminate (CSA) blending operates on a different time scale but with an analogous logic: Moelich et al. [23] replaced a fraction of the Portland cement by a belite-CSA and reported a substantial reduction of the 3-hour free shrinkage and an improvement in buildability through accelerated structuration; higher replacement ratios caused a stiffening rate incompatible with the pumping cycle.

Taken together, neither MgO-based expansive agents nor CSA blending addresses the plastic-shrinkage regime directly through volumetric cancellation: MgO is kinetically too slow, and CSA acts mainly by accelerating strength gain so that the element withstands the tensile stresses that still develop. Both families are therefore best understood as acting through a kinetic mechanism, bringing forward the moment at which the material can resist shrinkage-induced stress.

7.4. Water-soluble polymers (PVA)

Water-soluble polymers such as polyvinyl alcohol (PVA) carry dense hydroxyl groups along their chains, which confer a strong affinity for water molecules [11]. When dissolved and incorporated in the fresh 3DCP mixture, PVA adsorbs pore water and retards its evaporation, thereby acting through the same mechanism as external curing but from within the material. Unlike external bio-films (§7.1), PVA incorporation can also modify the rheology and the structural build-up of the printable mixture, which constrains the dosage window. At a modest dosage (2 wt % of cement mass), Xia et al. reported that PVA reduces the 24-h plastic shrinkage by about 60% and the 24-h cumulative evaporation by about 70% under evaporative conditions comparable to those of §7.1.3 (Fig. 11). These values are of the same order as those obtained with the surface-sprayed NSSA of §7.1.3, but the mechanism and the deployment are distinct: PVA is incorporated at the mixing stage and cannot be adjusted in-line, whereas NSSA is a post-print surface treatment.

The suppression of plastic-shrinkage cracking observed in PVA-modified 3DCP partly follows from the reduced shrinkage strain itself, since a material that shrinks less is less likely to crack (Fig. 12). A distinct mechanical contribution becomes visible only when the comparison is made at equal cumulative mass loss. Under the evaporative conditions tested, the mass loss reached by the reference 3DCP at 2 h corresponds to that reached by the PVA-modified 3DCP at 24 h. At this matched mass loss, the reference material exhibits approximately twice the shrinkage strain of the PVA-modified one, and the reference surface shows a visibly propagated crack, whereas the PVA-modified surface remains uncracked. Once the contribution of the reduced shrinkage is accounted for in this way, the residual crack resistance reflects a distinct mechanism. Dehydration of the PVA emulsion leaves behind a toughening polymer network that bridges the cementitious matrix at a length scale much smaller than that of microfibers. The resulting architecture can be described as a polymer-cementitious hybrid (PCH) process, in which one additive contributes simultaneously to water retention and to post-cracking capacity. This combined action places PVA incorporation between pure moisture-control strategies (§7.1) and pure mechanical reinforcement (§7.3).

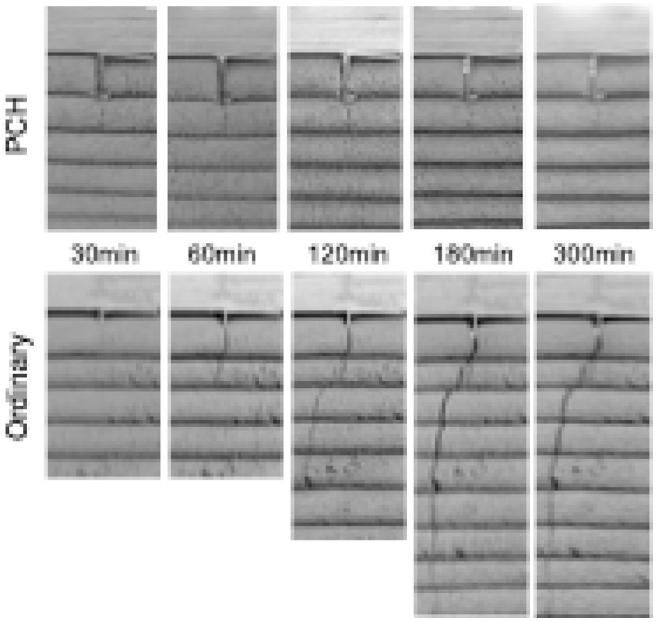


Fig. 12. Crack-resisting effect of PVA emulsion incorporated in 3DCP material top: PVA addition, bottom ordinary 3D mix.

7.5. Process and design-based mitigation

In addition to material-based strategies discussed in Sections 7.1 through 7.4, process- and design-based mitigations address the mechanical boundary conditions. These strategies acknowledge that some volumetric contraction is often unavoidable in 3DCP due to the large surface-to-volume ratio and binder content. Therefore, they interrupt the causal chain by managing mechanical restraint and geometric compatibility, ensuring that drying-induced strains do not translate into tensile stresses that exceed the material strength.

7.5.1. Geometric design

The geometric design of a printed component sets the level of mechanical restraint opposing free shrinkage, and therefore conditions the transition from strain to stress, independently of the underlying material behavior. For curved elements, a decreasing radius of curvature increases curvature-induced restraint, because self-equilibrating circumferential stresses resist free contraction [102]. In non-axisymmetric geometries, such as elliptical rings, the continuously varying local radius produces a spatially non-uniform shrinkage along the perimeter. Circumferential continuity is an additional geometric factor: opening a

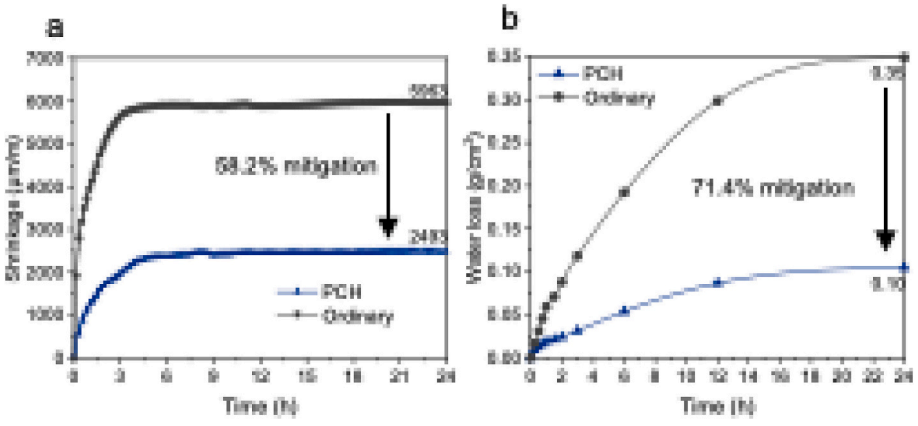


Fig. 11. Water-retaining and shrinkage mitigation effect of PVA emulsion incorporated in 3DCP material during 24 h after printing completion; (a) Plastic shrinkage (c) Water loss.

closed circular ring into an arc of progressively smaller angular extent relaxes the geometric constraint and allows free contraction to develop instead of stress [103]. At the design stage, mitigation for curved printed structures therefore reduces to managing the balance between local radius of curvature, circumferential compatibility, and the evolving tensile strength of the material [104]. The surface-to-volume ratio is a second geometric parameter with first-order influence: thin-walled printed sections expose a larger proportion of their volume to evaporation, and both the water loss and the drying-induced shrinkage scale accordingly, whereas thicker, multi-filament cross-sections redistribute the moisture gradient and slow the contraction of the core [10].

7.5.2. Process parameters and substrate interaction

At the process level, three parameters dominate the risk of cracking. The construction rate sets the overburden pressure experienced by the lower layers, which simultaneously enhances their capillary pressure and imposes restraint-induced tensile stresses once the self-weight exceeds the local tensile capacity [61]. The inter-layer time interval controls both the degree of drying of the exposed surface before burial and the extent of thermal coupling between freshly deposited and older layers [10,61]. Crucially, the base layer experiences kinematic confinement due to its interaction with the printing substrate: a rigid print bed imposes longitudinal restraint, and high interfacial friction concentrates tensile stresses at the base, which are experimentally linked to the location of the first shrinkage cracks [13]. Reducing the interfacial friction, for example, by using oiled plastic sheets or low-adhesion interlayers, lowers the shear transfer to the substrate, allows the base layer to contract, and produces nearly uniform layer-wise strains that suppress crack initiation [105]. Active environmental control at the printing stage, maintaining elevated ambient humidity or applying controlled water misting, complements these geometric and process measures and targets the evaporation-driven contribution identified in Section 2.

8. Conclusion and research directions

Printable cementitious materials are intrinsically more vulnerable to early-age drying than cast concrete. In the absence of formwork, the full perimeter of each deposited filament is exposed to the surrounding atmosphere immediately after deposition, producing surface-to-volume ratios one to two orders of magnitude greater than those of conventional structural elements. This geometric amplification is compounded by the high paste volumes required for extrudability and buildability, which concentrate drying-induced deformation in the most shrinkage-prone phase of the composite. In accelerated set-on-demand (2 K) systems, the rapid structuration further shortens the period during which viscous relaxation can dissipate capillary stresses, allowing damage to initiate before significant tensile resistance has developed; although the concurrent rapid gain in stiffness and strength may partially offset this vulnerability, so that the net effect for a given accelerated formulation remains an open question.

The unified physical framework proposed in this review links evaporation rate, capillary pressure build-up, macroscopic shrinkage and crack initiation through the competition between the evaporative flux J_e and the capillary supply flux J_{cap}. This framework provides a physically grounded basis for interpreting and predicting drying-induced damage across a wide range of printable formulations, geometries and processing conditions.

Recent advances in experimental techniques now enable multi-scale characterization of drying and shrinkage phenomena with a level of detail that was not accessible a decade ago. Gravimetric monitoring and laser displacement sensors capture global water loss and uniaxial macroscopic deformation, while digital image correlation (DIC) resolves the full-field strain localization at sub-millimeter resolution. Distributed fiber-optic sensing (FOS) extends strain measurement into the interior of the printed element, allowing deformation to be tracked within and across layers during and after deposition. Near-infrared (NIR) hyperspectral imaging provides spatially resolved maps, while miniature tensiometers enable direct measurement of capillary pressure evolution within fresh cementitious materials. Collectively, these complementary techniques make it possible to reconstruct the complete sequence from water loss to strain localization and crack initiation, providing quantitative validation of the proposed physical framework.

The distinction between two damage regimes (distributed surface cracklets in soft, freshly deposited materials and propagating macrocracks in stiffer, partially set materials) helps clarify the forms of damage expected as a function of formulation and age. Early-age creep and stress relaxation provide a temporary protective mechanism by dissipating part of the eigenstresses and restraint-induced stresses before the tensile strength threshold is reached; however, this protection diminishes rapidly as hydration and granular percolation proceed. The consequences of early-age drying extend well beyond the fresh state, including incomplete near-surface hydration, coarsened and more connected pore networks, reduced compressive and flexural strengths, impaired interlayer bonding, and anisotropic transport properties that govern long-term durability. The interlayer interface is particularly vulnerable, as drying of the exposed filament surface during the resting periods between layer depositions can produce cold joints that subsequently act as preferential pathways for carbonation and chloride ingress. Although this review has focused primarily on the mechanisms and consequences of early-age drying, the associated microstructural alterations have direct implications for the long-term durability of printed structures, and their systematic assessment remains an important objective for the field.

Several major research gaps emerge from this synthesis.

First, modeling of early-age behavior in 3DCP geometries remains fragmented. Validated coupled models integrating drying kinetics, hydration, poromechanical response, and viscoelastic relaxation under realistic printing schedules and boundary conditions are still lacking. During the first hours after deposition, the material transitions rapidly from a viscous suspension to a quasi-brittle solid, making the definition of constitutive laws particularly challenging. Capturing the coupling between drying-induced loading and the continuously evolving rheological and mechanical properties remains a major unresolved problem. Existing approaches typically address isolated parts of the causal chain; a predictive assessment of cracking risk in printed concretes requires their integration within unified multi-physics frameworks.

Second, experimental data linking controlled early-age drying histories to long-term performance remain scarce. The recent standardization efforts initiated by RILEM TC 304-ADC provide an important foundation for systematic investigation, but long-term durability datasets for printed elements subjected to quantified drying histories are still largely unavailable.

Third, curing protocols specifically adapted to the 3DCP process have not yet been standardized. Effective curing in printable systems must remain compatible with continuous deposition, multi-sided exposure, and the rheological constraints of printable mixtures. The mitigation strategies reviewed in this article, including external curing films, biofilms, internal curing agents, shrinkage-reducing admixtures, and process-level interventions, demonstrate that effective solutions exist across multiple stages of the drying-to-cracking chain. However, integrating these approaches into coherent, process-compatible curing strategies remains an important engineering challenge.

The evidence assembled in this review supports a clear practical conclusion: curing should be integrated into 3DCP process design from the outset rather than applied retrospectively after damage has occurred. The physical framework and the experimental methods presented here provide the basis for rational curing design in which the curing intensity and duration are matched to both the evaporative demand and the formulation-specific vulnerability window. At the current state of the evidence, the most robust results are obtained by combining surface evaporation control which addresses the driving force itself,

with short microfibers, which limit crack propagation. Internal strategies are promising but currently constrained by narrower dosage windows and by their coupling with the rheological requirements of printing. This hierarchy reflects the still-limited and heterogeneous evidence base rather than a definitive ranking. Addressing the remaining challenges will require advances in at least three areas: the development of coupled multi-physics models linking transport, hydration, and mechanics at the scale of printed elements; the generation of long-term durability datasets under controlled early-age drying conditions; and the implementation of automated, process-integrated curing strategies. Achieving the objectives will require interdisciplinary collaboration across porous-media physics, cement chemistry, computational mechanics, and process engineering.

CRediT authorship contribution statement

E. Keita: Writing – review & editing, Writing – original draft, Methodology, Formal analysis, Conceptualization. **L. Denis:** Writing – original draft. **H. Lombois-Burger:** Writing – review & editing, Writing – original draft. **S. Markin:** Writing – original draft, Methodology. **Y. Weng:** Writing – review & editing, Writing – original draft. **R. Wolfs:** Writing – review & editing, Writing – original draft. **K. Xia:** Writing – review & editing, Writing – original draft, Data curation. **M. Yang:** Writing – review & editing, Writing – original draft. **W. Yang:** Writing – review & editing, Writing – original draft, Data curation. **Q. Zhang:** Writing – review & editing, Writing – original draft, Methodology. **W. Zuo:** Writing – review & editing, Writing – original draft. **V. Mechtcherine:** Writing – review & editing, Writing – original draft, Methodology. **N. Roussel:** Writing – review & editing, Writing – original draft, Methodology.

Declaration of competing interest

The authors declare that they have no known competing financial interests or personal relationships that could have appeared to influence the work reported in this paper.

Acknowledgements

E. K. acknowledges funding from DURETERRE (ANR-22-CE22-0013) projects by the French National Research Agency (ANR).

Y. W. acknowledges funding from Research Grants Council of the Hong Kong Special Administrative Region, China (Project Reference Number: STG5/E-103/24-R).

V. M. acknowledges funding from the Deutsche Forschungsgemeinschaft (DFG, German Research Foundation) under Germany's Excellence Strategy – EXC 3115 – 533767731.

Data availability

Data will be made available on request.

References

[1] G. Habert, S.A. Miller, V.M. John, J.L. Provis, A. Favier, A. Horvath, K. L. Scrivener, Environmental impacts and decarbonization strategies in the cement and concrete industries, Nat. Rev. Earth Environ. 1 (2020) 559–573, https://doi.org/10.1038/s43017-020-0093-3.

[2] E. Elhacham, L. Ben-Uri, J. Grozovski, Y.M. Bar-On, R. Milo, Global human-made mass exceeds all living biomass, Nature 588 (2020) 442–444, https://doi.org/10.1038/s41586-020-3010-5.

[3] N. Roussel, Rheological requirements for 3D printing concrete, Cem. Concr. Res. 112 (2018) 102–112.

[4] T. Wangler, N. Roussel, F.P. Bos, T.A.M. Salet, R.J. Flatt, Digital concrete: a review, Cem. Concr. Res. 123 (2019) 105780, https://doi.org/10.1016/j.cemconres.2019.105780.

[5] W. Zuo, L. Caneda-Martinez, E. Keita, P. Aimedieu, M. Bornert, N. Roussel, Drying-induced damages in exposed fresh cement-based materials at very early ages: from standard casting to 3D printing, Cem. Concr. Res. 185 (2024) 107614, https://doi.org/10.1016/j.cemconres.2024.107614.

[6] L.E. Bryne, A. Ansell, J. Holmgren, Investigation of restrained shrinkage cracking in partially fixed shotcrete linings, Tunn. Undergr. Space Technol. 42 (2014) 136–143, https://doi.org/10.1016/j.tust.2014.02.011.

[7] Y. Wang, C. Shi, Y. Ma, Y. Xiao, Y. Liu, Accelerators for shotcrete – chemical composition and their effects on hydration, microstructure and properties of cement-based materials, Construct. Build. Mater. 281 (2021) 122557, https://doi.org/10.1016/j.conbuildmat.2021.122557.

[8] S. Markin, R. Combrinck, V. Mechtcherine, Specifics of plastic shrinkage in 3D-printed concrete elements, Cem. Concr. Res. 184 (2024) 107512, https://doi.org/10.1016/j.cemconres.2024.107512.

[9] E. Keita, Y. Rifaai, P. Belin, N. Roussel, Influence of non-adsorbing polymers on drying of fresh mortars, Cem. Concr. Res. 116 (2019) 38–44, https://doi.org/10.1016/j.cemconres.2018.10.016.

[10] L. Ma, Z. Jia, Y. Chen, Y. Jiang, B. Huet, A. Delaplace, Y. Zhang, Q. Zhang, Water loss and shrinkage prediction in 3D printed concrete with varying w/c and specimen sizes, Cem. Concr. Compos. 149 (2024) 105523, https://doi.org/10.1016/j.cemconcomp.2024.105523.

[11] H. Els, G. Van Zijl, W. De Villiers, A review of shrinkage and restrained shrinkage cracking in 3D concrete printing, J. Build. Eng. 111 (2025) 113233, https://doi.org/10.1016/j.jobe.2025.113233.

[12] Y. Tao, A.V. Rahul, K. Lesage, Y. Yuan, K. Van Tittelboom, G. De Schutter, Stiffening control of cement-based materials using accelerators in inline mixing processes: Possibilities and challenges, Cem. Concr. Compos. 119 (2021) 103972, https://doi.org/10.1016/j.cemconcomp.2021.103972.

[13] G.M. Moelich, J. Kruger, R. Combrinck, Plastic shrinkage cracking in 3D printed concrete, Compos. Part B Eng. 200 (2020) 108313, https://doi.org/10.1016/j.compositesb.2020.108313.

[14] S. Ghourchian, M. Butler, M. Krüger, V. Mechtcherine, Modelling the development of capillary pressure in freshly 3D-printed concrete elements, Cem. Concr. Res. 145 (2021) 106457, https://doi.org/10.1016/j.cemconres.2021.106457.

[15] Qi Zhang, H. Lombois-Burger, ViliaSprint2, the first on-site 3D-printed residential building in France: learnings for the construction sector, 2026. In Preparation.

[16] F.H. Wittmann, On the action of capillary pressure in fresh concrete 8 (1978) 565–570.

[17] S. Ghourchian, M. Wyrzykowski, P. Lura, A poromechanics model for plastic shrinkage of fresh cementitious materials, Cem. Concr. Res. 109 (2018) 120–132, https://doi.org/10.1016/j.cemconres.2018.04.013.

[18] W.P. Boshoff, R. Combrinck, Modelling the severity of plastic shrinkage cracking in concrete, Cem. Concr. Res. 48 (2013) 34–39, https://doi.org/10.1016/j.cemconres.2013.02.003.

[19] O.M. Jensen, P.F. Hansen, Autogenous deformation and RH-change in perspective, Cem. Concr. Res. 31 (2001) 1859–1865, https://doi.org/10.1016/S0008-8846(01)00501-4.

[20] G.W. Scherer, Drying, shrinkage, and cracking of cementitious materials, Transp. Porous Media 110 (2015) 311–331, https://doi.org/10.1007/s11242-015-0518-5.

[21] I. Maruyama, N. Kishi, A. Aili, The relative humidity range for the development of irreversible shrinkage in hardened cement paste, ACT 19 (2021) 585–592, https://doi.org/10.3151/jact.19.585.

[22] C. Liu, N. Banthia, Y. Shi, Z. Jia, Y. Zhang, Y. Chen, Y. Xiong, C. Chen, Early age shrinkage mitigation and quantitative study on water loss kinetics of 3D printed foam concrete modified with superabsorbent polymers, Addit. Manuf. 94 (2024) 104448, https://doi.org/10.1016/j.addma.2024.104448.

[23] G.M. Moelich, P.J. Kruger, R. Combrinck, Mitigating early age cracking in 3D printed concrete using fibres, superabsorbent polymers, shrinkage reducing admixtures, B-CSA cement and curing measures, Cem. Concr. Res. 159 (2022) 106862, https://doi.org/10.1016/j.cemconres.2022.106862.

[24] J. Van Der Putten, D. Snoeck, R. De Coensel, G. De Schutter, K. Van Tittelboom, Early age shrinkage phenomena of 3D printed cementitious materials with superabsorbent polymers, J. Build. Eng. 35 (2021) 102059, https://doi.org/10.1016/j.jobe.2020.102059.

[25] S. Ghourchian, M. Wyrzykowski, P. Lura, A poromechanics model for plastic shrinkage of fresh cementitious materials, Cem. Concr. Res. 109 (2018) 120–132.

[26] V. Baroghel-Bouny, M. Mainguy, T. Lassabatere, O. Coussy, Characterization and identification of equilibrium and transfer moisture properties for ordinary and high-performance cementitious materials, Cem. Concr. Res. 29 (1999) 1225–1238, https://doi.org/10.1016/S0008-8846(99)00102-7.

[27] G.W. Scherer, Theory of drying, J. Am. Ceram. Soc. 73 (1990) 3–14, https://doi.org/10.1111/j.1151-2916.1990.tb05082.x.

[28] P. Coussot, Scaling approach of the convective drying of a porous medium, Eur. Phys. J. B 15 (2000) 557–566, https://doi.org/10.1007/s100510051160.

[29] E. Keita, S.A. Koehler, P. Faure, D.A. Weitz, P. Coussot, Drying kinetics driven by the shape of the air/water interface in a capillary channel, The European physical journal. E, Soft matter 39 (2016) 23, https://doi.org/10.1140/epje/i2016-16023-8.

[30] P.-G. de Gennes, F. Brochard-Wyart, D. Quere, Capillarity and Wetting Phenomena: Drops, Bubbles, Pearls, Waves, 2004.

[31] E. Keita, T.E. Kodger, P. Faure, S. Rodts, D.A. Weitz, P. Coussot, Water retention against drying with soft-particle suspensions in porous media, Phys. Rev. E 94 (2016) 033104, https://doi.org/10.1103/PhysRevE.94.033104.

[32] F. Chauvet, P. Duru, S. Geoffroy, M. Prat, Three periods of drying of a single square capillary tube, Phys. Rev. Lett. 103 (2009) 1–4, https://doi.org/10.1103/PhysRevLett.103.124502.

[33] A.G. Yiotis, D. Salin, E.S. Tajer, Y.C. Yortsos, Drying in porous media with gravity-stabilized fronts: experimental results, Phys. Rev. E Stat. Nonlinear Soft Matter Phys. 86 (2012) 026310, https://doi.org/10.1103/PhysRevE.86.026310.
[34] N. Shokri, D. Or, What determines drying rates at the onset of diffusion controlled stage-2 evaporation from porous media? Water Resour. Res. 47 (2011) 1–8, https://doi.org/10.1029/2010WR010284.
[35] H. Darcy, Les fontaines publiques de la ville de Dijon: Exposition et application des principes à suivre et des formules à employer dans les questions de distribution d'eau, Victor Dalmont, éditeur, Paris, 1856.
[36] I. Chatzis, F. Dullien, Modelling pore structure by 2-D and 3-D networks with application to sandstones, J. Can. Pet. Technol. 16 (1977) 97–108, https://doi.org/10.2118/77-01-09.
[37] M. Suzuki, S. Maeda, On the mechanism of drying of granular beds: mass transfer from discontinuous source, J. Chem. Eng. Jpn. 1 (1968) 26–31, https://doi.org/10.1252/jcej.1.26.
[38] S. Ghourchian, M. Wyrzykowski, P. Lura, The bleeding test: a simple method for obtaining the permeability and bulk modulus of fresh concrete, Cem. Concr. Res. 89 (2016) 249–256, https://doi.org/10.1016/j.cemconres.2016.08.016.
[39] A. Gribonval, M. Pierre, N. Ducoulombier, K. Sab, R. Mesnil, J. Bleyer, Multi-physics modelling of 3D-printed concrete evolution in environmental conditions, Cem. Concr. Res. 196 (2025) 107918, https://doi.org/10.1016/j.cemconres.2025.107918.
[40] N. Massoussi, E. Keita, N. Roussel, The heterogeneous nature of the bleeding phenomenon in cement paste, Cem. Concr. Res. 95 (2017) 108–116, https://doi.org/10.1016/j.cemconres.2017.02.012.
[41] A. Perrot, T. Lecompte, H. Khelifi, C. Brumaud, J. Hot, N. Roussel, Yield stress and bleeding of fresh cement pastes, Cem. Concr. Res. 42 (2012) 937–944, https://doi.org/10.1016/j.cemconres.2012.03.015.
[42] C. Zhang, V.N. Nerella, A. Krishna, S. Wang, Y. Zhang, V. Mechtcherine, N. Banthia, Mix design concepts for 3D printable concrete: a review, Cem. Concr. Compos. 122 (2021) 104155, https://doi.org/10.1016/j.cemconcomp.2021.104155.
[43] Y. Chen, S. Chaves Figueiredo, Z. Li, Z. Chang, K. Jansen, O. Çopuroğlu, E. Schlangen, Improving printability of limestone-calcined clay-based cementitious materials by using viscosity-modifying admixture, Cem. Concr. Res. 132 (2020) 106040, https://doi.org/10.1016/j.cemconres.2020.106040.
[44] C.A. Menzel, Causes and Prevention of Crack Development in Plastic Concrete, 1954.
[45] P.J. Uno, Plastic shrinkage cracking and evaporation formulae, ACI Mater. J. 95 (1998). http://www.concrete.org/Publications/ACIMaterialsJournal/ACIJournalSearch.aspx?m=details&ID=379.
[46] ACI 305, ACI 305R-99 hot weather concreting reported by ACI committee 305, J. Am. Concr. Inst. (2000) 1–20.
[47] G.M. Moelich, J.E. Van Zyl, N. Rabie, R. Combrinck, The influence of solar radiation on plastic shrinkage cracking in concrete, Cem. Concr. Compos. 123 (2021) 104182, https://doi.org/10.1016/j.cemconcomp.2021.104182.
[48] V.N. Nerella, S. Hempel, V. Mechtcherine, Effects of layer-interface properties on mechanical performance of concrete elements produced by extrusion-based 3D-printing, Construct. Build. Mater. 205 (2019) 586–601, https://doi.org/10.1016/j.conbuildmat.2019.01.235.
[49] E. Keita, H. Bessaies-Bey, W. Zuo, P. Belin, N. Roussel, Weak bond strength between successive layers in extrusion-based additive manufacturing: measurement and physical origin, Cem. Concr. Res. 123 (2019) 105787, https://doi.org/10.1016/j.cemconres.2019.105787.
[50] L. Josserand, O. Coussy, F. De Larrard, Bleeding of concrete as an ageing consolidation process, Cem. Concr. Res. 36 (2006) 1603–1608, https://doi.org/10.1016/j.cemconres.2004.10.006.
[51] M. Pierre, M. Samudio, S. Ghabezloo, P. Dangla, Modelling the poromechanical behaviour of class G cement paste: a multiphysics approach from early age to hardened state, Cem. Concr. Res. 193 (2025) 107852, https://doi.org/10.1016/j.cemconres.2025.107852.
[52] S. Ghourchian, M. Wyrzykowski, M. Plamondon, P. Lura, On the mechanism of plastic shrinkage cracking in fresh cementitious materials, Cem. Concr. Res. 115 (2019) 251–263, https://doi.org/10.1016/j.cemconres.2018.10.015.
[53] J. Versteege, R.J.M. Wolfs, T.A.M. Salet, Data-driven additive manufacturing with concrete: enhancing in-line sensory data with domain knowledge, Part II: moisture and heat, Autom. Constr. 177 (2025) 106327, https://doi.org/10.1016/j.autcon.2025.106327.
[54] L. Ptacek, A. Strauss, B. Hinterstoisser, A. Zitek, Curing assessment of concrete with hyperspectral imaging, Materials (Basel, Switzerland) 14 (2021) 3848, https://doi.org/10.3390/ma14143848.
[55] D. Gastaldi, F. Canonico, S. Irico, D. Pellerej, M.C. Paganini, Near-infrared spectroscopy investigation on the hydration degree of a cement paste, J. Mater. Sci. 45 (2010) 3169–3174, https://doi.org/10.1007/s10853-010-4323-9.
[56] M. Ghandehari, C.S. Vimer, I. Ioannou, A. Sidelev, W. Jin, P. Spellane, In-situ measurement of liquid phase moisture in cement mortar, NDT & E Int. 45 (2012) 162–168, https://doi.org/10.1016/j.ndteint.2011.09.011.
[57] A. Watanabe, H. Furukawa, S. Miyamoto, H. Minagawa, Non-destructive chemical analysis of water and chlorine content in cement paste using near-infrared spectroscopy, Construct. Build. Mater. 196 (2019) 95–104, https://doi.org/10.1016/j.conbuildmat.2018.11.114.
[58] S. Rath, Y. Sakai, Evaluation of the water penetration depth in mortar using water indicator and hyperspectral imaging, Construct. Build. Mater. 380 (2023) 131269, https://doi.org/10.1016/j.conbuildmat.2023.131269.
[59] S. Li, Y. Sakai, Rapid visualization and quantification of water penetration into cement paste using near-infrared hyperspectral imaging, Cem. Concr. Compos. 161 (2025) 106103, https://doi.org/10.1016/j.cemconcomp.2025.106103.
[60] K. Xia, Y. Chen, Z. Zhang, W. Wang, Y. Chen, L. Jia, Z. Jia, S. Quan, Y. Zhang, In-situ crosslinked nano SiO2 reinforced alginate bio-textile for mitigating plastic shrinkage in 3D printed concrete, Addit. Manuf. 102 (2025) 104753, https://doi.org/10.1016/j.addma.2025.104753.
[61] K. Xia, Y. Chen, Y. Chen, Z. Jia, L. Jia, Y. Gao, Y. Zhang, Understanding and modeling the plastic deformation of 3D printed concrete based on viscoelastic creep behavior, Addit. Manuf. 84 (2024) 104132, https://doi.org/10.1016/j.addma.2024.104132.
[62] X. Han, J. Yan, T. Chen, B. Tang, Y. Lin, Plastic shrinkage of 3D printed concrete under different self-weight of upper layers, Construct. Build. Mater. 399 (2023) 132564, https://doi.org/10.1016/j.conbuildmat.2023.132564.
[63] B. Pan, K. Qian, H. Xie, A. Asundi, Two-dimensional digital image correlation for in-plane displacement and strain measurement: a review, Meas. Sci. Technol. 20 (2009) 062001, https://doi.org/10.1088/0957-0233/20/6/062001.
[64] S. Markin, V. Mechtcherine, Quantification of plastic shrinkage and plastic shrinkage cracking of the 3D printable concretes using 2D digital image correlation, Cem. Concr. Compos. 139 (2023) 105050, https://doi.org/10.1016/j.cemconcomp.2023.105050.
[65] Y. Yao, M. Yan, Y. Bao, Measurement of cable forces for automated monitoring of engineering structures using fiber optic sensors: a review, Autom. Constr. 126 (2021) 103687, https://doi.org/10.1016/j.autcon.2021.103687.
[66] X. Tan, A. Abu-Obeidah, Y. Bao, H. Nassif, W. Nasreddine, Measurement and visualization of strains and cracks in CFRP post-tensioned fiber reinforced concrete beams using distributed fiber optic sensors, Autom. Constr. 124 (2021) 103604, https://doi.org/10.1016/j.autcon.2021.103604.
[67] M.F. Bado, J.R. Casas, A. Dey, C.G. Berrocal, G. Kaklauskas, I. Fernandez, R. Rempling, Characterization of concrete shrinkage induced strains in internally-restrained RC structures by distributed optical fiber sensing, Cem. Concr. Compos. 120 (2021) 104058, https://doi.org/10.1016/j.cemconcomp.2021.104058.
[68] H. Zhang, L. Hao, S. Zhang, J. Xiao, C.S. Poon, Advanced measurement techniques for plastic shrinkage and cracking in 3D-printed concrete utilising distributed optical fiber sensor, Addit. Manuf. 74 (2023) 103722, https://doi.org/10.1016/j.addma.2023.103722.
[69] S. Markin, M. Schmidt, S. Zhang, D. Käßler, M. Eiserbeck, G. Bausch, In-situ monitoring and controlling of plastic shrinkage in 3D-printed concrete elements, in: 5th RILEM International Conference on Concrete and Digital Fabrication, 2026.
[70] S. Markin, J.A.L. Cordova, V. Mechtcherine, Evolution of capillary pressure in 3D-printed concrete elements: numerical modelling and experimental validation, Construct. Build. Mater. 409 (2023) 133677, https://doi.org/10.1016/j.conbuildmat.2023.133677.
[71] H. Ogura, V.N. Nerella, V. Mechtcherine, Developing and testing of strain-hardening cement-based composites (SHCC) in the context of 3D-printing, Materials (Basel, Switzerland) 11 (2018) 1375, https://doi.org/10.3390/ma11081375.
[72] Q. Wang, X. Ren, J. Li, Damage-rheology model for predicting 3D printed concrete buildability, Autom. Constr. 155 (2023), https://doi.org/10.1016/j.autcon.2023.105037.
[73] P. Saravanan, A. Ramaswamy, Early age creep behavior of 3D printable mortar: Hydration and viscoelasticity coupling model, Mech. Mater. 211 (2025) 105484, https://doi.org/10.1016/j.mechmat.2025.105484.
[74] Z. Chang, M. Liang, Y. Chen, E. Schlangen, B. Šavija, Does early age creep influence buildability of 3D printed concrete? Insights from numerical simulations, Addit. Manuf. 77 (2023) 1–15, https://doi.org/10.1016/j.addma.2023.103788.
[75] V. Slowik, M. Schmidt, R. Fritzsch, Capillary pressure in fresh cement-based materials and identification of the air entry value, Cem. Concr. Compos. 30 (2008) 557–565, https://doi.org/10.1016/j.cemconcomp.2008.03.002.
[76] G.W. Scherer, Drying of Gels: V Rigid Gels 92, 1987, pp. 122–144.
[77] C.W. Macminn, E.R. Dufresne, J.S. Wettlaufer, Large deformations of a soft porous material, Phys. Rev. Appl. 5 (2016) 1–30, https://doi.org/10.1103/PhysRevApplied.5.044020.
[78] J.R. Rice, Thermodynamics of the quasi-static growth of Griffith cracks, J. Mech. Phys. Solids 26 (1978) 61–78, https://doi.org/10.1016/0022-5096(78)90014-5.
[79] J.G. Sanjayan, B. Nematollahi, M. Xia, T. Marchment, Effect of surface moisture on inter-layer strength of 3D printed concrete, Construct. Build. Mater. 172 (2018) 468–475, https://doi.org/10.1016/j.conbuildmat.2018.03.232.
[80] L. Ma, Q. Zhang, Z. Jia, C. Liu, Z. Deng, Y. Zhang, Effect of drying environment on mechanical properties, internal RH and pore structure of 3D printed concrete, Construct. Build. Mater. 315 (2022) 125731.
[81] R.J. Flatt, G.W. Scherer, J.W. Bullard, Why alite stops hydrating below 80% relative humidity, Cem. Concr. Res. 41 (2011) 987–992.
[82] L. Ma, Q. Zhang, H. Lombois-Burger, Z. Jia, Z. Zhang, G. Niu, Y. Zhang, Pore structure, internal relative humidity, and fiber orientation of 3D printed concrete with polypropylene fiber and their relation with shrinkage, J. Build. Eng. 61 (2022) 105250.
[83] G.M. Moelich, P.J. Kruger, R. Combrinck, Mitigating early age cracking in 3D printed concrete using fibres, superabsorbent polymers, shrinkage reducing admixtures, B-CSA cement and curing measures, Cem. Concr. Res. 159 (2022) 106862.
[84] R.J.M. Wolfs, F.P. Bos, A.S.J. Salet, Mechanical properties of 3D printed concrete in the fresh state, Cem. Concr. Res. 122 (2019) 118–129.

[85] G.M. Moelich, J. Kruger, R. Combrinck, Modelling the interlayer bond strength of 3D printed concrete with surface moisture, Cem. Concr. Res. 150 (2021) 106559, https://doi.org/10.1016/j.cemconres.2021.106559.
[86] K. Xia, Y. Chen, Q. Yu, Y. Zhang, Plastic deformation induced non-uniform global distribution of microstructure and related performances within 3D printed concrete, Cem. Concr. Compos. 170 (2026) 106598, https://doi.org/10.1016/j.cemconcomp.2026.106598.
[87] L. de Lima, T. Wangler, Y. Zhang, K. Van Tittelboom, G. De Schutter, V. Mechtcherine, F.P. Bos, Recommendation of RILEM TC 304-ADC for durability testing of cementitious materials produced through extrusion-based additive manufacturing (3D concrete printing, 3DCP), 2026. Submitted.
[88] Y. Zhang, L.N. De Lima, D. Böhler, A. Arunothayan, A.J. Babafemi, B. Baz, L. Caneda-Martinez, G. De Schutter, H. Du, N. Freund, Y. Gao, L. Hanžič, S. Jain, Z. Jiang, E. Keita, D. Lowke, I. Mai, S. Muthukrishnan, Q. Ren, A. Sapata, M. Sinka, C. Snguanyat, K. Šter, J. Van Der Putten, Z. Wang, T. Wangler, K. Van Tittelboom, Durability assessment of 3D printed cement-based materials: a RILEM TC 304-ADC interlaboratory study, Mater. Struct. 58 (2025) 314, https://doi.org/10.1617/s11527-025-02797-5.
[89] J.D. Malan, A.S. Van Rooyen, G.P.A.G. Van Zijl, Chloride induced corrosion and carbonation in 3D printed concrete, Infrastructures 7 (2021) 1, https://doi.org/10.3390/infrastructures7010001.
[90] K. Van Tittelboom, M.K. Mohan, B. Šavija, E. Keita, G. Ma, H. Du, J. Kruger, L. Caneda-Martinez, L. Wang, M. Bekaert, T. Wangler, Z. Wang, V. Mechtcherine, N. Roussel, On the micro- and meso-structure and durability of 3D printed concrete elements, Cem. Concr. Res. 185 (2024) 107649, https://doi.org/10.1016/j.cemconres.2024.107649.
[91] J. Van Der Putten, M. De Volder, P. Van Den Heede, M. Deprez, V. Cnudde, G. De Schutter, K. Van Tittelboom, Transport properties of 3D printed cementitious materials with prolonged time gap between successive layers, Cem. Concr. Res. 155 (2022) 106777, https://doi.org/10.1016/j.cemconres.2022.106777.
[92] F.P. Bos, Y. Zhang, S. Muthukrishan, L. de Lima, G. De Schutter, K. Van Tittelboom, R.J.M. Wolfs, C. Menna, V. Mechtcherine, Recommendation of RILEM TC 304-ADC for the preparation of specimens for mechanical and durability testing of cementitious materials produced through extrusion-based additive manufacturing (3D concrete printing, 3DCP), 2026. Submitted.
[93] S. Markin, Understanding and mitigating plastic shrinkage in 3D-printed concrete elements: = Untersuchung und Vorbeugung des plastischen Schwindens in 3D-gedruckten Betonelementen, Technische Universität Dresden, 2024.
[94] M. Wyrzykowski, S.-I. Igarashi, P. Lura, V. Mechtcherine, Recommendation of RILEM TC 260-RSC: using superabsorbent polymers (SAP) to mitigate autogenous shrinkage, Mater. Struct. 51 (2018) 135, https://doi.org/10.1617/s11527-018-1241-9.
[95] Y. Chen, S. He, Y. Zhang, Z. Wan, O. Çopuroğlu, E. Schlangen, 3D printing of calcined clay-limestone-based cementitious materials, Cem. Concr. Res. 149 (2021) 106553, https://doi.org/10.1016/j.cemconres.2021.106553.
[96] F. Rajabipour, G. Sant, J. Weiss, Interactions between shrinkage reducing admixtures (SRA) and cement paste's pore solution, Cem. Concr. Res. 38 (2008) 606–615, https://doi.org/10.1016/j.cemconres.2007.12.005.
[97] D.P. Bentz, M.R. Geiker, K.K. Hansen, Shrinkage-reducing admixtures and early-age desiccation in cement pastes and mortars, Cem. Concr. Res. 31 (2001) 1075–1085, https://doi.org/10.1016/S0008-8846(01)00519-1.
[98] G. Sant, P. Lura, J. Weiss, Measurement of volume change in cementitious materials at early ages: review of testing protocols and interpretation of results, Transp. Res. Rec. J. Transp. Res. Board 1979 (2006) 21–29, https://doi.org/10.1177/0361198106197900104.
[99] J. Mora-Ruacho, R. Gettu, A. Aguado, Influence of shrinkage-reducing admixtures on the reduction of plastic shrinkage cracking in concrete, Cem. Concr. Res. 39 (2009) 141–146, https://doi.org/10.1016/j.cemconres.2008.11.011.
[100] L. Ma, Q. Zhang, Z. Jia, C. Liu, Z. Deng, Y. Zhang, Effect of drying environment on mechanical properties, internal RH and pore structure of 3D printed concrete, Construct. Build. Mater. 315 (2022) 125731, https://doi.org/10.1016/j.conbuildmat.2021.125731.
[101] Y. Chen, L. Zhang, K. Wei, H. Gao, Z. Liu, Y. She, F. Chen, H. Gao, Q. Yu, Rheology control and shrinkage mitigation of 3D printed geopolymer concrete using nanocellulose and magnesium oxide, Construct. Build. Mater. 429 (2024) 136421, https://doi.org/10.1016/j.conbuildmat.2024.136421.
[102] A.B. Hossain, J. Weiss, Assessing residual stress development and stress relaxation in restrained concrete ring specimens, Cem. Concr. Compos. 26 (2004) 531–540, https://doi.org/10.1016/S0958-9465(03)00069-6.
[103] C. Tian, Z. Dong, X. Wei, The investigation of shrinkage cracking of paste and mortar based on the eccentric ring test and multiphysics simulation, Construct. Build. Mater. 408 (2023) 133579, https://doi.org/10.1016/j.conbuildmat.2023.133579.
[104] Z. Qu, Y. Zhang, Z. Liu, R. Si, J. Wu, A review on early-age cracking of concrete: causes and control, Case Stud. Constr. Mater. 21 (2024) e03848, https://doi.org/10.1016/j.cscm.2024.e03848.
[105] A.K. Patel, A. Tripathi, R. Kiran, M. Santhanam, G. Sant, N. Neithalath, Decoupling early-age free shrinkage and restraint effects in 3D printed concrete using digital image correlation, Cem. Concr. Compos. 166 (2026) 106405, https://doi.org/10.1016/j.cemconcomp.2025.106405.